

Contents lists available at ScienceDirect

Petroleum Science

journal homepage: www.keaipublishing.com/en/journals/petroleum-science



Original Paper

Coupling mechanism analysis of CO₂ non-Darcy flow in multi-scale reservoirs: A case study of the life-cycle process of fracturing-development in shale oil reservoirs



Zhen-Hua Rui ^{a, b}, Hai-Yang Deng ^{a, b}, Ting Hu ^{a, b, *}, Guang-Long Sheng ^{c, d}, Malcolm Wilson ^e, Birol Dindoruk ^f, Shirish Patil ^g

- ^a State Key Laboratory of Petroleum Resources and Engineering, China University of Petroleum (Beijing), Beijing, 102249, China
- ^b College of Petroleum Engineering, China University of Petroleum (Beijing), Beijing, 102249, China
- ^c School of Petroleum Engineering, Yangtze University, Wuhan, 430100, Hubei, China
- d Hubei Key Laboratory of Oil and Gas Drilling and Production Engineering (Yangtze University), Wuhan, 430100, Hubei, China
- ^e Clean Energy Technologies Research Institute (CETRI), University of Regina, 3737 Wascana Parkway, Regina, SK, S4S 0A2, Canada
- ^f Petroleum Engineering & Chemical and Biomolecular Engineering, University of Houston, Houston, TX, 77004, USA
- g Department of Petroleum Engineering, King Fahd University of Petroleum and Minerals, Dhahran, 31261, Saudi Arabia

ARTICLE INFO

Article history: Received 11 July 2024 Received in revised form 16 December 2024 Accepted 19 December 2024 Available online 24 December 2024

Edited by Yan-Hua Sun

Keywords: Shale oil reservoir Life-cycle simulation Multiple mechanism coupling Non-Darcy flow CCUS-EOR

ABSTRACT

With policy support for carbon capture, utilization, and storage (CCUS), an integrated approach that combines energy storage fracturing, CO₂-enhanced oil recovery (EOR), and storage emerges as a promising direction for the shale oil industry. The process of energy storage fracturing induces significant changes in the pressure and saturation of the medium. However, conventional simulations often overlook the effects of fracturing and shut-in operations on the seepage field and production performance. Furthermore, fractured shale reservoirs exhibit complex non-Darcy flow characteristics due to intricate pore structures and multi-scale porous media. A comprehensive understanding of flow mechanisms is essential for effective reservoir development and CO₂ storage. This study establishes a multi-component simulation model that encompasses the life-cycle of fracturing, shut-in, production, and CO2 huff-n-puff processes, thereby ensuring the continuity of the seepage field. The model accounts for the effect of nano-confinement on phase behavior by modifying the equation of state. Furthermore, the flux term is adjusted to incorporate Maxwell-Stefan diffusion, pre-/post-Darcy flow, and stress sensitivity. The embedded discrete fracture model (EDFM) is employed to simulate multiphase flow within multi-scale media, and the results from the validation model align satisfactorily with those derived from ECLIPSE. Mechanism analysis indicates that the interaction of multiple mechanisms significantly influences both production and storage performance. Under the multi-mechanism coupling, the cumulative oil production increased by 12.01%, while the utilization and storage factors increased by 62.93% and 8.93%, respectively. The role of molecular diffusion in shale oil reservoirs may be overstated, contributing only a 0.26% enhancement in oil production. Simulation results show that the energy storage fracturing strategy can increase oil production and net present value by 12.47% and 15.07%, respectively. Sensitivity analysis indicates that the CO2 injection rate is the main factor affecting the recovery factor, followed by CO2 injection time and the number of cycles, with fracturing fluid volume having the least impact. This study develops a multi-process, multi-mechanism simulation framework for multi-scale shale oil reservoirs. This framework provides a robust evaluation system for CCUS-EOR, facilitating informed decisionmaking in fracturing stimulation, development planning, and parameter optimization.

© 2024 The Authors. Publishing services by Elsevier B.V. on behalf of KeAi Communications Co. Ltd. This is an open access article under the CC BY-NC-ND license (http://creativecommons.org/licenses/by-nc-nd/

4.0/).

1. Introduction

Shale oil is abundant in resources, and its economical and efficient exploitation can help alleviate current energy shortages (Singh and Cai, 2018). Shale formations have very small pore

Corresponding author.

E-mail address: huting@cup.edu.cn (T. Hu).

throats (from micrometers to nanometers) and ultra-low permeability (from micro-Darcy to nano-Darcy). Therefore, multi-stage fractured horizontal wells (MFHWs) technology is used to obtain industrial production capacity (Zhao et al., 2023). Due to the characteristics of reservoirs, production rates decline rapidly in later stages, and the primary recovery is low, particularly when the original formation energy is insufficient (Wang et al., 2017). Therefore, improving the recovery factor of shale oil reservoirs is of crucial for extending the production cycle.

The main energy supplementation methods in shale reservoirs are energy storage fracturing and CO₂-EOR (tertiary recovery). Studies indicate that energy storage fracturing can mitigate production decline rates when compared to immediate flowback post-fracturing (Zhang et al., 2017). Furthermore, existing studies suggest that CO₂ huff-n-puff more applies to shale reservoirs than continuous CO₂ flooding and CO₂ water-alternating-gas (Liu et al., 2023). Recent pilot tests have confirmed the feasibility of CO₂ huff-n-puff in shale oil reservoirs for enhancing oil recovery while also achieving carbon sequestration (Zhao et al., 2022). The detailed mechanism of CO₂ recovery and storage in shale reservoirs is referred to the work of Hu et al. (2023).

The injection of fracturing fluid during the fracturing period and oil—water replacement during the shut-in period significantly affect the pressure and saturation distribution before production (Sheng et al., 2023a). However, existing CO_2 huff-n-puff simulations rarely consider the effects of fracturing and shut-in periods on the seepage field and production performance. Therefore, it is necessary to establish an integrated simulation model for the life-cycle of fracturing, shut-in, production, and CO_2 huff-n-puff to accurately evaluate production and storage performance.

In recent years, researchers have made many achievements in the integrated modeling of fracturing, shut-in, and production (Fakcharoenphol et al., 2016). Wang et al. (2022) established a multi-process oil-water black oil model for fracturing, shut-in, and production in shale oil reservoirs. The purpose is to determine the optimal shut-in time after multi-stage multi-cluster fracturing. However, the model used the equivalent property method to characterize fractures, which posed challenges in accurately capturing the flow relationship between the matrix and the fractures. Sheng et al. (2023a) developed an integrated gas-water model for shale gas reservoir fracturing, shut-in, and production. The model used the DPDK-EDFM to characterize the multiple media, including the organic matrix, inorganic matrix, and natural/ hydraulic fractures. However, so far, there is no literature that can achieve integrated simulation of energy storage fracturing and CO₂ huff-n-puff.

The full-cycle simulation faces two significant challenges. The first challenge is the physical mechanism during energy storage fracturing period. Numerous fracture propagation models exist to calculate fracture length and aperture. These models include twodimensional (2D) planar fracture propagation models, such as the Perkins-Khristianovic-Nordgren (PKN) model Khristianovic-Geertsma-De Klerk (KGD) model (Geertsma and De Klerk, 1969). Additionally, there are also 2D fracture network models, like the lightning breakdown simulation model (Sheng et al., 2023b). Dontsov and Peirce (2017) developed a 3D fracture propagation model that considers viscous, toughness, and leak-off effects. During the shut-in period, the high-energy fracturing fluid migrates into the matrix, which enhances formation energy and alleviate the water-locking effect (Zhang et al., 2017).

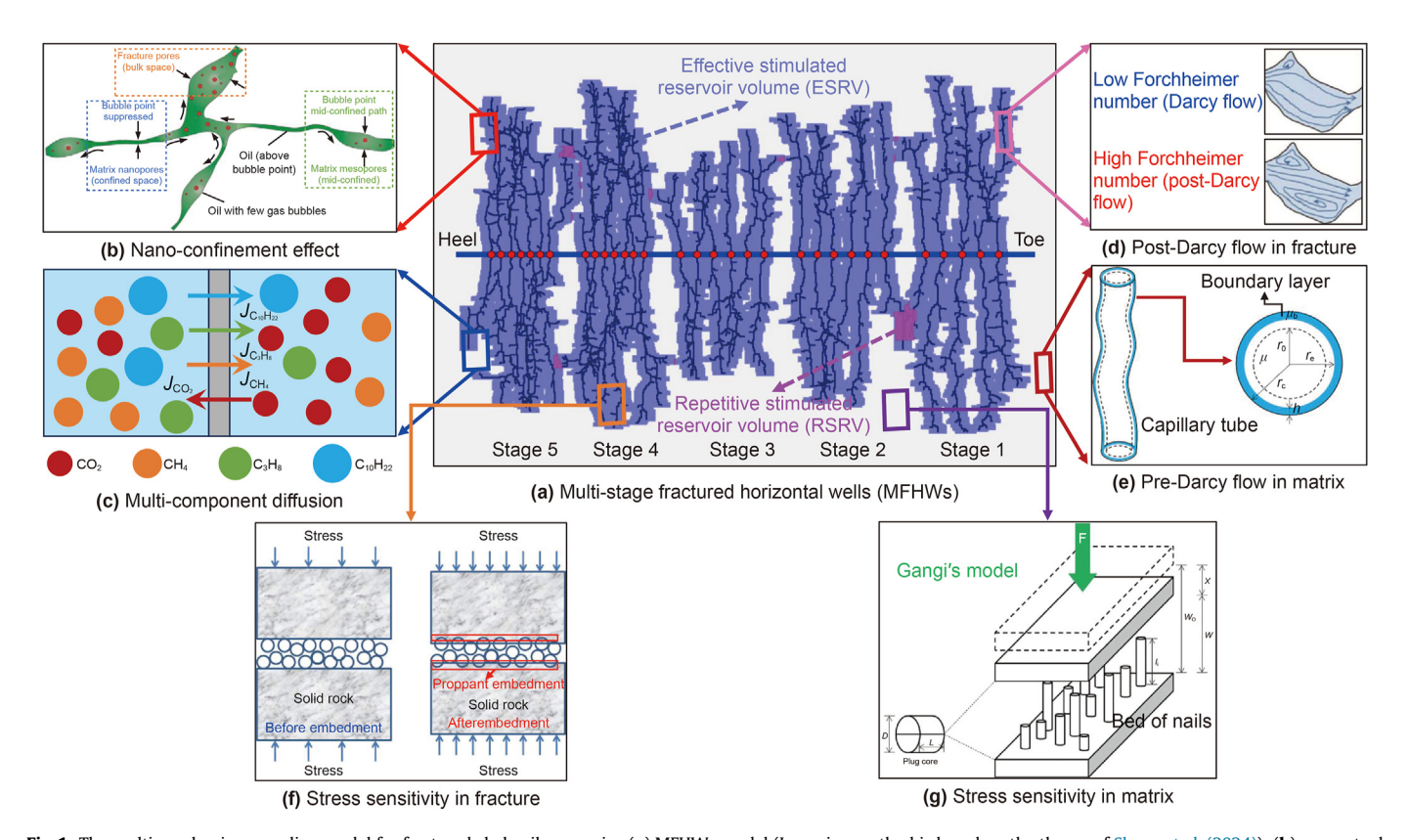


Fig. 1. The multi-mechanism coupling model for fractured shale oil reservoirs. (a) MFHWs model (Inversion method is based on the theory of Sheng et al. (2024)); (b) conceptual pore network model (Alharthy et al., 2013); (c) schematic of multi-component diffusion; (d) Darcy flow and post-Darcy flow within the fracture domain (Niu et al., 2022; Shao et al., 2020); (e) schematic of fluid distribution in a capillary tube (Cheng et al., 2023); (f) schematic of proppant embedment (Chen et al., 2017); (g) schematic of Gangi's model (Wasaki and Akkutlu, 2015).

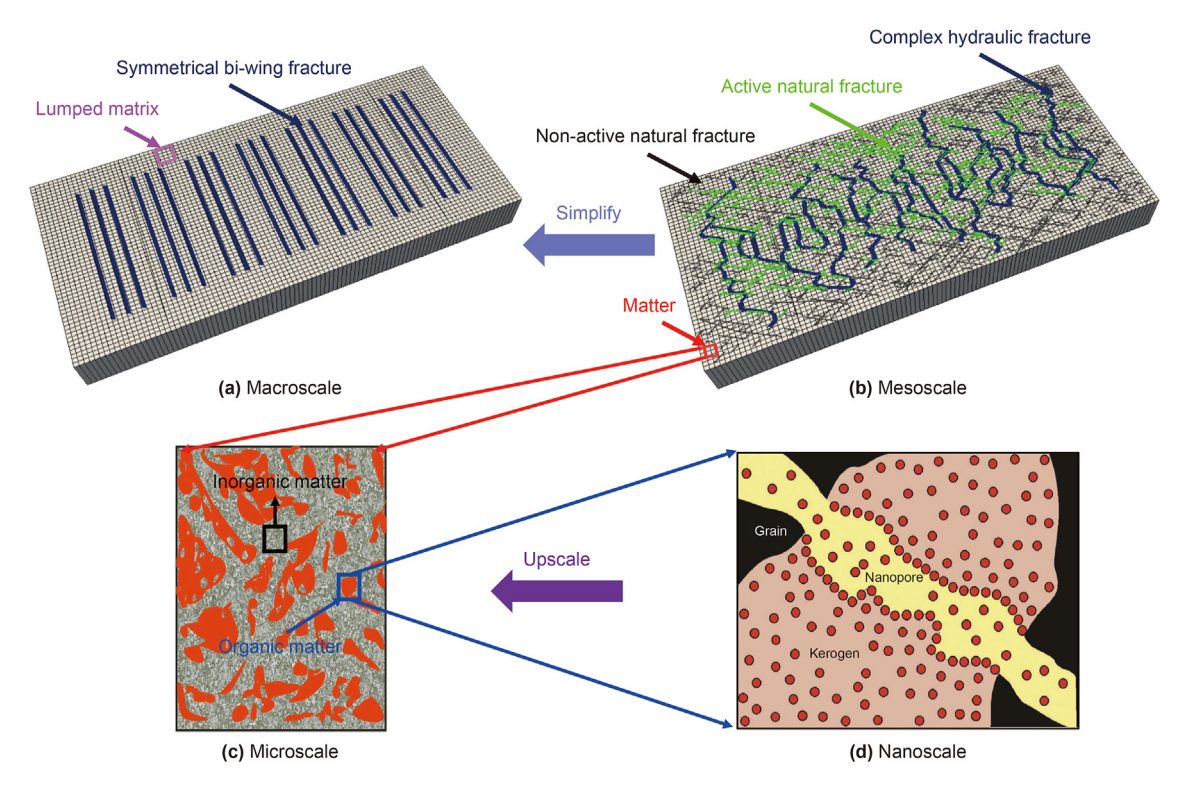


Fig. 2. Schematic of physical models at different scales: (a) bi-wing fracture model at the macroscale (Yu et al., 2018); (b) hydraulic/natural fracture network model at the mesoscale (Yu et al., 2018); (c) organic/inorganic matter model at the microscale; (d) schematic of nanopore fluid transport in organic matter at the nanoscale (Javadpour, 2009).

Furthermore, the fracture dynamics resulting from partial closure impact production behavior (Zhang and Emami-Meybodi, 2020a). Zhang and Emami-Meybodi (2020b) used a robust semi-analytical model for accurate characterization. To further consider the fracture damage effect, Zhang et al. (2024) proposed an innovative type-curve method to estimate fracture properties. This method showed a much closer match with flowback history and more accurate interpretation results than previous methods.

The second challenge is the multi-mechanism coupling in the development process of shale oil reservoirs, as illustrated in Fig. 1. For the single-factor mechanism, current theoretical understanding of the nano-confinement effect (Yu et al., 2019), pre-Darcy flow (Wang et al., 2020), post-Darcy flow (Azin and Izadpanahi, 2022), and stress sensitivity (Wang and Fidelibus, 2021) is relatively wellestablished, thus further elaboration is unnecessary. In shale gas reservoirs, the contribution of the diffusive flux to the total flux can be significant. However, the role of diffusion in oil-dominated shale reservoirs needs to be further evaluated. Sun et al. (2016) argued that molecular diffusion has little impact on the increase of production during CO₂ huff-n-puff in shale oil reservoirs. There are two main methods for addressing multi-mechanism coupling. The first category is the apparent permeability method (APM). For instance, Wu et al. (2016) developed a unified model for gas transfer coupling different gas-transfer mechanisms in nanopores. This model summarizes the effects of adsorption/desorption, slippage, Knudsen diffusion, surface diffusion, and stress sensitivity as changes in permeability. However, the APM method is typically applicable to single-component shale or coal rock gas (Rezaveisi et al., 2014). The second category is the direct modification method (DMM), which is a general method. Wang et al. (2024) established a multimechanism model for continuous CO2 flooding and storage in shale oil reservoirs. The model considers the influence of nano-pore structure on fluid phase behavior by modifying the equation of state, and modifies the multi-component conservation equation to

consider stress sensitivity and molecular diffusion. However, this model overlooks the significant differences in stress sensitivity between the matrix and hydraulic fracture media, using a single stress sensitivity mechanism to capture the pressure dependency. Moreover, the model does not consider the pre-Darcy flow in the matrix and post-Darcy flow in the fractures.

In response to the above challenges, this work developed a lifecycle multi-component simulation model that integrates a multicontinuous process, including fracturing, shut-in, depletion

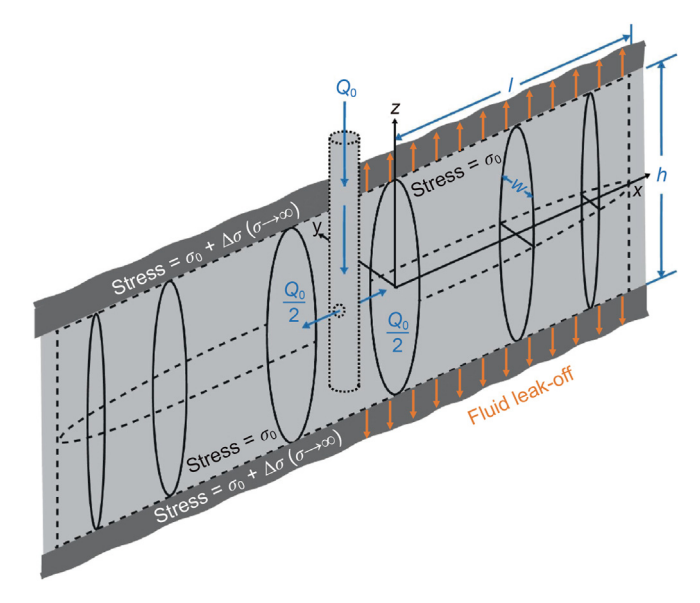


Fig. 3. Sketch of a bi-wing constant height hydraulic fracture (Zia and Lecampion, 2017).

production, and CO₂ huff-n-puff. Additionally, it incorporated a multi-mechanism framework that accounts for the nano-confinement effect, molecular diffusion, pre-/post-Darcy flow, and stress sensitivity. The model used the PKN-EDFM approach to characterize and simulate multi-stage, multi-cluster fractures in shale oil reservoirs. This model establishes a robust framework for accurately evaluating production and storage performance in CCUS-EOR processes. Section 2 details the methodology, including the introduction of the physical model, the physical mechanism of the full-cycle process, the construction of the EDFM, the discretization and solution of the control equations, and the establishment of a CCUS-EOR evaluation system. Section 3 is model validation and mechanism analysis. Section 4 discusses the impact of operating parameters on various evaluation indexes. Finally, Section 5 is the conclusion of the paper.

2. Methodology

2.1. Physical model and assumption

The shale system is a complex porous medium of inorganic matter, organic matter, and natural and artificial fractures (Sheng et al., 2023a). Organic matter and natural fractures are crucial in the occurrence and migration of oil and gas. However, they are too small to quantify adequately in the reservoir simulation. In practical studies, oil-wet organic matter, water-wet inorganic matter, and natural fractures are usually considered lumped matrix (Wang et al., 2009). The lumped matrix exhibits mixed wettability characteristics. Furthermore, as illustrated in Fig. 2, complex fracture networks are simplified into symmetrical bi-wing fractures.

We present the following assumptions to enhance the computational efficiency of multi-mechanism coupling modeling:

- (1) The reservoir maintains a constant temperature condition.
- (2) The fluid is divided into the water phase, oil (liquid) phase, and gas (vapor) phase. The water phase is immiscible. The phase equilibrium only considers the oil and gas phases.
- (3) This model does not consider the dissolution of CO₂ in water and the adsorption/desorption of CO₂ on rock surfaces.
- (4) Given the specified fracture geometry and properties, the fracture propagation process is simplified to the injection process.

2.2. Mass conservation equation

This paper proposes a mass-conservation governing equation incorporating the pre-/post-Darcy flow, stress sensitivity, and convection-diffusion transport. The subscripts L, V, and w denote the liquid (oil) phase, vapor (gas) phase, and aqueous (water) phase, respectively. The mass conservation equation of each component is defined as follows

$$\frac{\partial}{\partial t} \left[\phi \sum_{\alpha = \mathsf{L}, \mathsf{V}} \rho_{\alpha} \mathsf{S}_{\alpha} \mathsf{X}_{\alpha}^{i} \right] + \sum_{\alpha = \mathsf{L}, \mathsf{V}} \nabla \cdot \left(\rho_{\alpha} \mathsf{X}_{\alpha}^{i} \boldsymbol{v}_{\alpha} + J_{\alpha}^{i} \right) - \sum_{\alpha = \mathsf{L}, \mathsf{V}} \rho_{\alpha} \mathsf{X}_{\alpha}^{i} q_{\alpha} \middle/ \mathsf{V} = 0$$

Similarly, the mass conservation equation of the water phase in the fracture and matrix can be written as

$$\frac{\partial}{\partial t} (\phi \rho_{\mathsf{w}} S_{\mathsf{w}}) + \nabla \cdot (\rho_{\mathsf{w}} \mathbf{v}_{\mathsf{w}}) - \rho_{\mathsf{w}} q_{\mathsf{w}} / V = 0$$
 (2)

where ϕ represents porosity; ρ_{α} and S_{α} are the mass density and

saturation of the phase α , respectively; X^i_α is the mass fraction of component i in phase α ; J^i_α is the molecular diffusion mass flux, kg/ (m² s); $q_\alpha = q^{\rm well}_\alpha - q^{\rm mc}_\alpha$ is the volumetric flux, which is divided by pore volume V to maintain dimensional consistency. For the matrix, $q_\alpha = q^{\rm m}_\alpha - q^{\rm m,f}_\alpha$; for fractures, $q_\alpha = q^{\rm f}_\alpha - q^{\rm f,m}_\alpha - q^{\rm f,f}_\alpha$. Here, $q^{\rm m}_\alpha$ is the source/sink term in the matrix, $q^{\rm f}_\alpha$ is the source/sink term in the fracture, $q^{\rm m,f}_\alpha$ is the transfer function of each phase from the matrix to the fracture, $q^{\rm f,m}_\alpha$ is the transfer function of each phase from the fracture to the matrix, and $q^{\rm f_1,f_2}_\alpha$ is the transfer function of each phase from fracture 1 to fracture 2. The non-Darcy velocity \mathbf{v}_α , is defined as

$$\mathbf{v}_{\alpha} = -F_{\alpha} \frac{k k_{\Gamma,\alpha}}{\mu_{\alpha}} (\nabla P_{\alpha} - \rho_{\alpha} g \nabla z) = -F_{\alpha} k \lambda_{\alpha} \nabla \Phi$$

$$F_{\alpha} = f_{F,\alpha}^{\text{Post-Darcy}} f_{M,\alpha}^{\text{Pre-Darcy}} f_{F,\alpha}^{\text{Stress}} f_{M,\alpha}^{\text{Stress}}$$
(3)

where F_{α} is the non-Darcy correction factor; Φ is the potential gradient; $f_{{\rm F},\alpha}^{{\rm Post-Darcy}}$ and $f_{{\rm M},\alpha}^{{\rm Pre-Darcy}}$ are the pre-Darcy and post-Darcy flow correction factors, respectively; $f_{{\rm F},\alpha}^{{\rm Stress}}$ and $f_{{\rm M},\alpha}^{{\rm Stress}}$ are the stress sensitivity correction factors of fracture and matrix, respectively; k is the absolute permeability; $k_{{\rm r},\alpha}$ is the relative permeability of phase α ; μ_{α} and λ_{α} are the viscosity and mobility of phase α , respectively; g is the gravitational acceleration.

2.3. Physical mechanisms during the energy storage fracturing period

2.3.1. Fracturing period

A large amount of fracturing fluid is injected into the shale reservoir during the fracturing period. As the pressure of the fracturing fluid changes, the fracture aperture increases. This paper uses the PKN model to estimate both the fracture length and aperture based on the specified fracturing fluid displacement, viscosity, and mechanical properties (Yew and Weng, 2014).

Analytical approximations can be made in the two following limiting cases by introducing a dimensionless time (t_D), as defined by Nordgren (1972).

$$t_{\rm D} = \left[\frac{16C_{\rm L}^5 Ght^{3/2}}{(1 - \nu)\pi^3 \mu Q_0^2} \right]^{2/3} \tag{4}$$

When t_D < 0.01, the problem falls into a short-time regime, and the leak-off effect can be approximated (Yew and Weng, 2014).

$$\begin{cases} l = 0.68 \left[\frac{GQ_0^3}{(1 - \nu)\mu h^4} \right]^{1/5} t^{4/5} \\ w = 2.5 \left[\frac{(1 - \nu)\mu Q_0^2}{Gh} \right]^{1/5} t^{1/5} \end{cases}$$
(5)

Conversely, when $t_{\rm D} > 1$, the problem falls into a long-time regime dominated by the fluid leak-off (Yew and Weng, 2014), as shown in Fig. 3.

$$\begin{cases} l = \left(\frac{Q_0}{\pi C_L h}\right) t^{1/2} \\ w = 4 \left[\frac{2(1-v)\mu Q_0^2}{\pi^3 G C_L h}\right]^{1/4} t^{1/8} \end{cases}$$
 (6)

where h is the fracture height, ft; G is the bulk shear modulus, psi; v

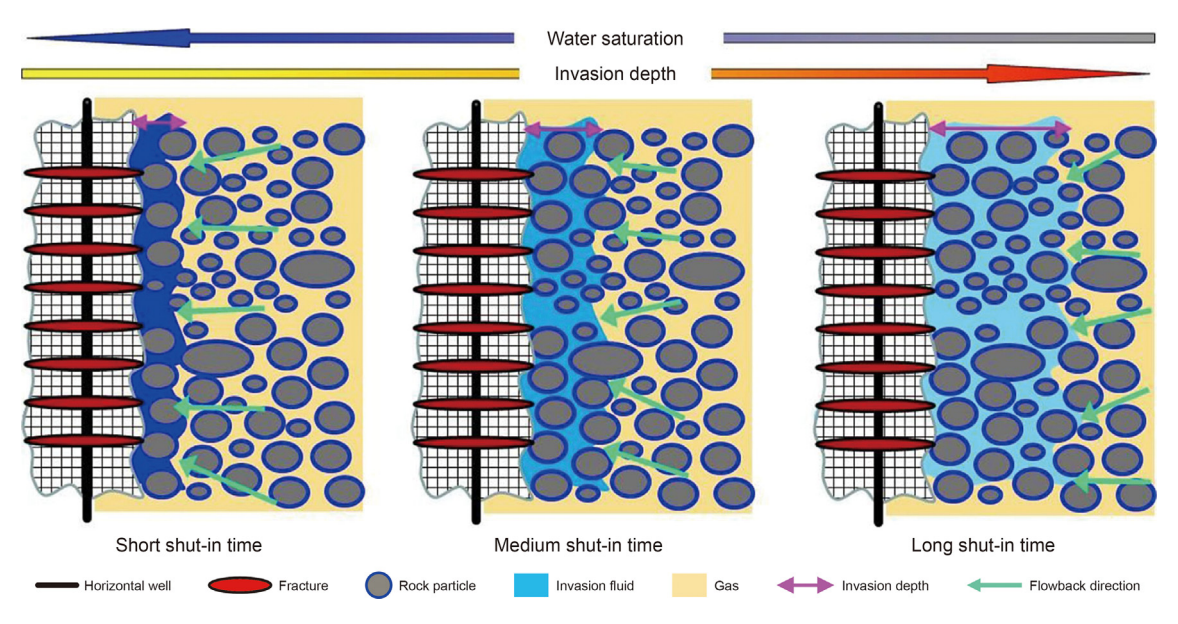


Fig. 4. Schematic of the changes in water saturation and invasion depth at different shut-in times (Zhang et al., 2017).

is the drained Poisson's ratio; μ is fracturing fluid viscosity, cP; C_L is the leak-off coefficient, ft/min^{0.5}; t is the injection time, min; Q_0 is the fracturing fluid volume for each stage, bbl/min. The fracture half-length (l) and fracture width (w) grow faster with time in the no leak-off case (Eq. (5)) than in the large leak-off case (Eq. (6)) (Nordgren, 1972).

After injecting fracturing fluid at each stage, fluid can flow through the settled proppant pack. The permeability k_p of an immobile proppant pack is characterized by the Kozeny–Carmen equation, as outlined by Huang et al. (2022).

$$k_{\rm p} = \frac{\left(sd_{\rm p}\right)^2}{K_{\rm c}} \frac{\phi_{\rm p}^3}{\left(1 - \phi_{\rm p}\right)^2} \tag{7}$$

where s denotes the grain shape factor; d_p is the proppant diameter; K_c is an empirical constant, K_c is generally set to 150 in the literature (Huang et al., 2022); ϕ_p is the porosity of particle pack. It can be derived from the maximum concentration of proppant.

$$\phi_{\mathbf{p}} = 1 - c_{\mathbf{s}} \tag{8}$$

where c_s is the maximum fraction of solids in a proppant packing (0.745 in this paper).

2.3.2. Shut-in period

During the post-fracturing shut-in period, the fracturing fluid leaks into the reservoir matrix due to the high-pressure gradient. Moreover, the shale matrix typically exhibits high capillary pressure. This leads to the spontaneous imbibition of fracturing fluid by the matrix, which enhances pressure transfer and mass exchange between the fractures and the matrix. The shut-in operation fulfills two essential roles: firstly, it increases the fluid pressure within the matrix pores, contributing to energy storage (Fakcharoenphol et al., 2016; Zhang et al., 2017). Secondly, the fracturing fluid migrates toward the unstimulated regions as shut-in time progresses. This process reduces water saturation in the fractures and the stimulated areas, which helps alleviate the water-locking effect (Zhang

et al., 2017). Fig. 4 illustrates the changes in water saturation and fluid invasion (leak-off) at different shut-in times.

2.4. Physical mechanisms during the development period

2.4.1. Phase equilibrium of mixtures in nanopores

Different from conventional reservoirs, the pore-throat size of shale is generally at the nanometer scale, as shown in Fig. 1(b). When the pore radius is less than 10 nm, the fluid properties and phase behavior will change significantly (Yu et al., 2019). The nanoconfinement effect mainly occurs due to the capillary pressure and the fluid—wall interaction (Song et al., 2021). Researchers have used the grand canonical Monte Carlo (GCMC) method to quantify the shift of the critical parameters and have developed a series of poresize-dependent formulas (Jia et al., 2023).

$$\Delta P_{\rm c}^* = \frac{P_{\rm cb} - P_{\rm cp}}{P_{\rm cb}} = 0.9409 \left(\frac{\sigma_{\rm LJ}}{r_{\rm p}}\right) - 0.2415 \left(\frac{\sigma_{\rm LJ}}{r_{\rm p}}\right)^2 \tag{9}$$

$$\Delta T_{\rm c}^* = \frac{T_{\rm cb} - T_{\rm cp}}{T_{\rm cb}} = 0.9409 \left(\frac{\sigma_{\rm LJ}}{r_{\rm p}}\right) - 0.2415 \left(\frac{\sigma_{\rm LJ}}{r_{\rm p}}\right)^2 \tag{10}$$

$$\sigma_{\rm LJ} = 0.244 \sqrt[3]{\frac{T_{\rm cb}}{P_{\rm cb}}} \tag{11}$$

where the subscripts cb and cp denote the bulk and confined space, respectively; $\Delta T_{\rm c}^*$ is the relative critical temperature shift, K; $\Delta P_{\rm c}^*$ is the relative critical temperature shift, atm; $r_{\rm p}$ is the pore-throat radius; $\delta_{\rm LJ}$ is the Lennard-Jones size parameter.

The equivalent pore radius of shale can be approximated using the Karmen–Kozeny correlation (Rezaveisi et al., 2014).

$$r_{\text{ave}} = 2\sqrt{2\tau}\sqrt{\frac{k}{\phi}} \tag{12}$$

where τ is the tortuosity of porous media. Shen and Chen (2007)

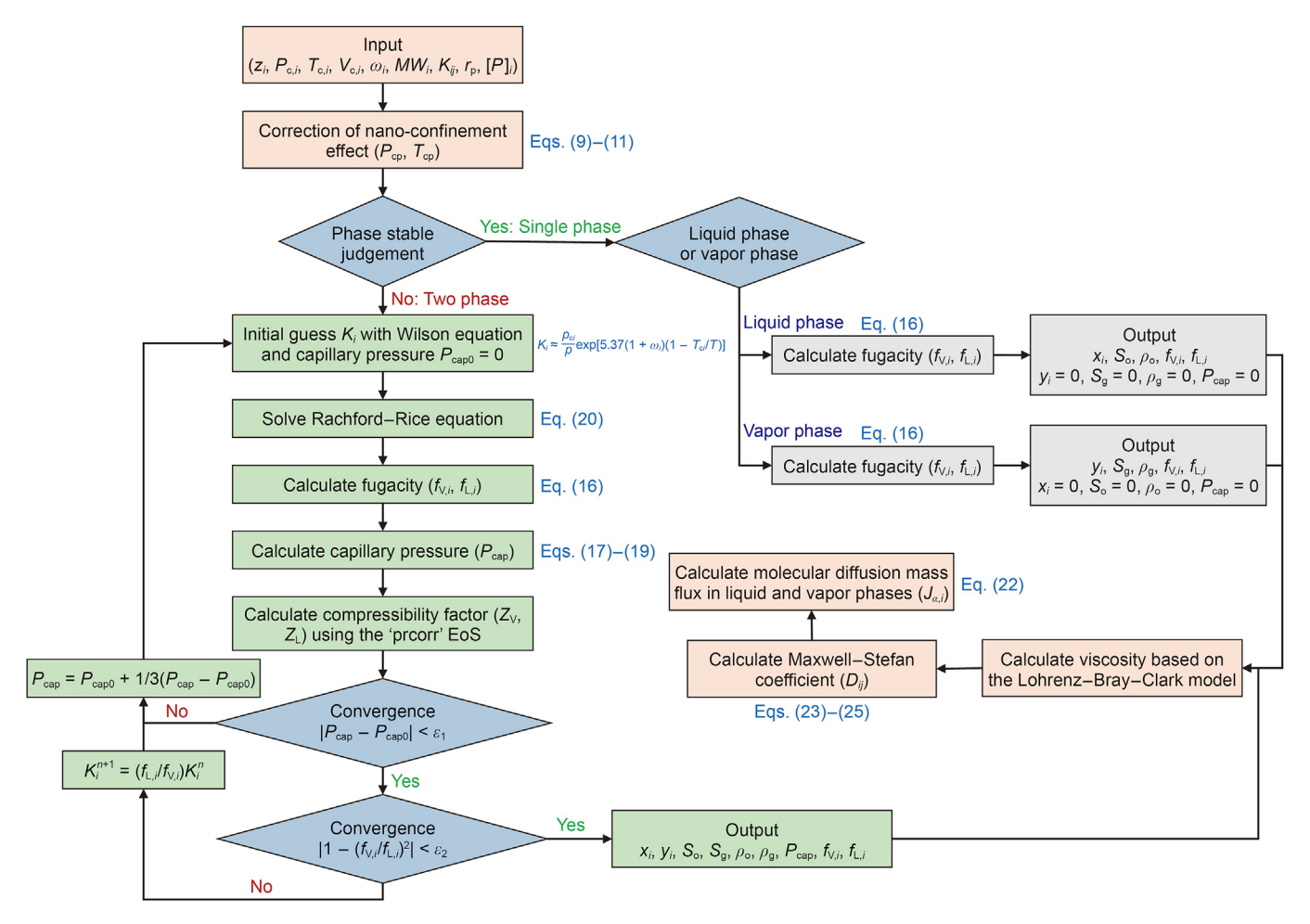


Fig. 5. Flow chart of gas-liquid equilibrium and parameter calculation (modified from Jia et al. (2023)).

summarized three types of tortuosity—porosity correlations. They pointed out that the error of the logarithmic relationship is the smallest.

$$\begin{cases} \tau = \left(A\phi^{1-m}\right)^n, \ A = n = 1 \text{ and } m = 2.14 \pm 0.02\\ \tau = \phi + B(1 - \phi), \ B = 3.79 \pm 0.10\\ \tau = 1 - C\ln\phi, \ C = 2.02 \pm 0.09 \end{cases}$$
(13)

The phase equilibrium also needs to satisfy the following auxiliary equations.

$$\sum_{i=1}^{N_c} z_i = \sum_{i=1}^{N_c} x_i = \sum_{i=1}^{N_c} y_i = 1, \quad i = 1, 2, \dots, N_c$$
 (14)

$$S_{w} + S_{o} + S_{g} = 1 ag{15}$$

$$f_{L,i}(T, P_L, x_i) = f_{V,i}(T, P_L + P_{cap}, y_i), \quad i = 1, 2, \dots, N_c$$
 (16)

where N_c is the total number of components; z_i is the mole fraction of component i; x_i and y_i are the mole fractions of component i in the liquid and vapor phases, respectively; $f_{L,i}$ and $f_{V,i}$ are the fugacity of component i in the liquid and vapor phases, respectively; T is the reservoir temperature; P_{cap} is the capillary pressure. P_{cap} can be included in the phase equilibrium calculation by the Young—Laplace equation (Poling et al., 2001).

$$P_{\mathsf{cap}} = P_{\mathsf{V}} - P_{\mathsf{L}} = \frac{2\sigma\mathsf{cos}\theta}{r_{\mathsf{p}}} \tag{17}$$

where θ is the contact angle, representing the angle between the pore surface and vapor—liquid interface; σ is the interface tension (IFT). The interfacial tension is estimated using the Parachor model (Poling et al., 2001).

$$\sigma^{1/E} = \sum_{i=1}^{N_c} \left(\overline{\rho}_{M}^{L}[P]_i x_i - \overline{\rho}_{M}^{V}[P]_i y_i \right)$$
(18)

where $[P]_i$ is the Parachor parameter of the pure component; E is the scaling exponent; $\overline{\rho}_{\rm M}^{\rm L}$ and $\overline{\rho}_{\rm M}^{\rm V}$ are the molar densities of the liquid and vapor phases, respectively. When the density unit is mol/cm³, the interfacial tension unit is D/cm. The scaling exponent E is typically 3.6 or 4.0. Danesh et al. (1991) pointed out that when E becomes a function of phase density, the accuracy of capillary pressure prediction can be improved. They noted that the Lee–Chien method has a lower error than the Weinaug–Katz method.

$$\begin{cases} E=3.535+17.76\Big(\overline{\rho}_{\rm M}^{\rm L}-\overline{\rho}_{\rm M}^{\rm V}\Big), & \text{Lee-Chien method} \\ E=3.583+0.16\Big(\overline{\rho}_{\rm M}^{\rm L}-\overline{\rho}_{\rm M}^{\rm V}\Big), & \text{Weinaug-Katz method} \end{cases}$$
 (19)

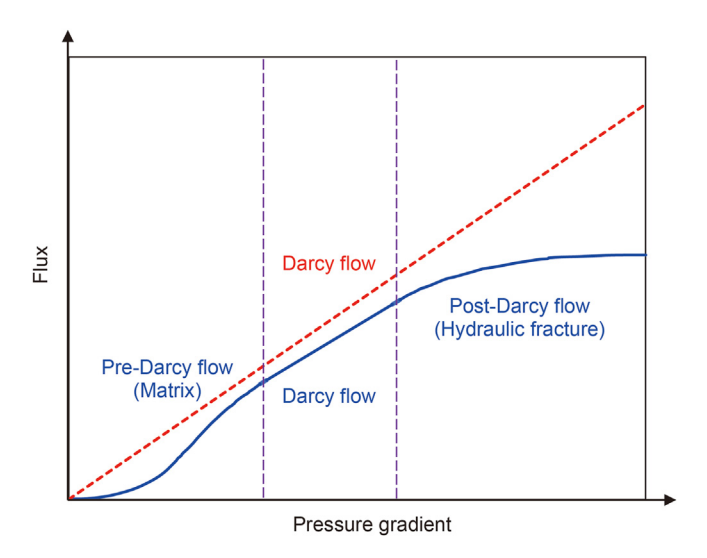


Fig. 6. Schematic of pre-Darcy flow and post-Darcy flow. In this study, both pre-Darcy flow and post-Darcy flow are observed to be smaller than the linear Darcy flow.

The vapor—liquid equilibrium is calculated using the Rachford—Rice formula (Lie and Møyner, 2021).

$$\begin{cases}
O_2 - O_1 = O_{RR} = \sum_{i=1}^{N_c} \frac{(K_i - 1)z_i}{1 + F_V(K_i - 1)} = 0 \\
K_i^{k+1} = K_i^k \frac{f_L(P, T, \mathbf{x}^k)}{f_V(P, T, \mathbf{y}^k)}, \quad x_i^k = \frac{z_i}{F_L + (1 - F_L)K_i^k}, \quad y_i^k = K_i^k x_i^k
\end{cases}$$
(20)

where O_1 , O_2 , and O_{RR} are the three objective functions; F_V is the vapor phase molar fraction; F_L is the liquid phase mole fraction; K_i is the equilibrium coefficient of component i; and the superscript k is the number of iterations. Eq. (20) can be calculated using the successive substitution iteration (SSI) or the Newton method. The flash procedure is detailed in the work of Lie and Møyner (2021). Fig. 5 presents the flow chart for calculating phase equilibrium, considering the nano-confinement effect, and labels the corresponding equations in the figure. Furthermore, the output results are also used to calculate the diffusion coefficient.

The corrected Peng—Robinson equation of state (PR-EOS) is used to calculate the compressibility factor $Z({\rm Martin}, 1979)$. Based on the Z-factors, the fugacity f and density ρ are subsequently derived. Typically, the EOS does not predict viscosity. The Lohrenz—Bray—Clark correlation (Lohrenz et al., 1964) is most commonly used to calculate the viscosity of hydrocarbon mixtures. In a three-phase system, the oil phase and gas phase saturation are obtained using the following equation.

$$S_{o} = (1 - S_{w}) \frac{Z_{L} F_{L}}{Z_{L} F_{L} + Z_{V} (1 - F_{L})}$$
 (21)

2.4.2. Maxwell-Stefan diffusion

It is essential to accurately evaluate the contribution of diffusion flux to the total flux during the soaking and production periods. The existing literature often assumes that the diffusion coefficient of each component remains constant (Ratnakar and Dindoruk, 2022; Sun et al., 2015). However, studies have shown that the diffusion coefficient is inversely proportional to pressure (Olorode et al.,

2017). This work uses the generalized Maxwell—Stefan diffusion model to estimate the diffusion coefficients under varying pressures and compositions. Taylor and Krishna (1993) gave the multicomponent diffusion flux equation in the tortuous porous medium.

$$J_{\alpha}^{i} = -\frac{\phi S_{\alpha}}{\tau} D_{\alpha}^{i} \nabla \left(\rho_{\alpha} X_{\alpha}^{i} \right), \ D_{\alpha}^{i} = \left(\mathbf{B}_{\alpha}^{i} \right)^{-1} \Gamma_{\alpha} = \mathbf{D}_{\alpha}^{i} \Gamma_{\alpha}$$
 (22)

where the product $\rho_{\alpha}X_{\alpha}$ is the mass concentration of component i in phase α . Eq. (22) shows that diffusion flux is driven by the mass concentration of the hydrocarbon components in each phase. Olorode et al. (2021) also discussed that diffusion flux is driven by concentration gradient (Fig. 1(c)) and chemical potential gradient. $\textbf{\textit{B}}$ is the drag matrix; $\textbf{\textit{D}}$ is the Maxwell—Stefan diffusion coefficient matrix. The main diagonal elements in $\textbf{\textit{D}}$ represent the self-diffusion ability of each component, while the off-diagonal elements reflect the magnitude of intermolecular interactions. There is no reciprocal relationship between off-diagonal elements.

Olorode et al. (2021) provided the definition of the thermodynamic factor matrix, denoted as Γ .

$$\Gamma^{\alpha}_{ij} = \delta_{ij} + x^{i}_{\alpha} \frac{\partial \ln \varphi^{i}_{\alpha}}{\partial x^{j}_{\alpha}} \bigg|_{TP\Sigma} = \frac{x^{i}_{\alpha}}{f^{i}_{\alpha}} \frac{\partial f^{i}_{\alpha}}{\partial x^{j}_{\alpha}}, \quad \varphi^{i}_{\alpha} = \frac{f^{i}_{\alpha}}{x^{i}_{\alpha}P}$$
(23)

where δ_{ij} is the Kronecker function; φ is the fugacity coefficient. The partial derivative in this equation is carried out at isobaric and isothermal conditions. The symbol Σ indicates that $\ln \varphi$ is differentiated to mole fraction while keeping the mole fractions of all other species, except for the n-th, constant. The Jacobian matrix of fugacity can be obtained using the compositional module in MAT-LAB Reservoir Simulation Toolbox (MRST) (Lie and Møyner, 2021).

Taylor and Krishna (1993) provided the equation for obtaining the drag matrix **B**.

$$\begin{cases}
B_{ii} = \frac{x_{\alpha}^{i}}{D_{in}} + \sum_{k=1}^{N_{c}} \frac{x_{\alpha}^{k}}{D_{ik}}, (i, j = 1, 2, ..., N_{c} - 1); B_{ii}^{N_{c}} = \sum_{k=1}^{N_{c}} \frac{x_{\alpha}^{k}}{D_{ik}} \\
B_{ij} = -x_{\alpha}^{i} \left(\frac{1}{D_{ij}} - \frac{1}{D_{in}}\right), (i, j = 1, 2, ..., N_{c} - 1); B_{ij}^{N_{c}} = -\frac{x_{\alpha}^{i}}{D_{ij}}, \text{ for } i \neq j
\end{cases}$$
(24)

where D_{ij} , D_{in} , and D_{ik} are the Maxwell–Stefan diffusion coefficient for any pair of components. This paper used the Fuller empirical correlation to calculate the diffusion coefficient of binary systems (Fuller et al., 2002).

$$D_{AB} = \frac{10^{-3} T^{1.75} (1/M_A + 1/M_B)^{0.5}}{P \left[(\sum V_A)^{1/3} + (\sum V_B)^{1/3} \right]^2}$$
(25)

where P is the pore pressure, atm; M_i is the molecular weight of the component, g/mol; D_{AB} is the diffusion coefficient of binary systems, cm²/s; T is the temperature, K; ΣV_i is the the sum of the diffusion volumes of the component i.

2.4.3. Pre-/post-Darcy flow

The highly conductive fractures in shale oil reservoirs provide high-velocity flow channels for fluids. As the flow rate increases, inertial forces become more significant. It leads to a nonlinear relationship between the pressure gradient and seepage velocity, as shown in Fig. 6. When the Forchheimer number (Fo) in the fracture is high (e.g., Fo > 0.11), the classical Darcy's law is no longer

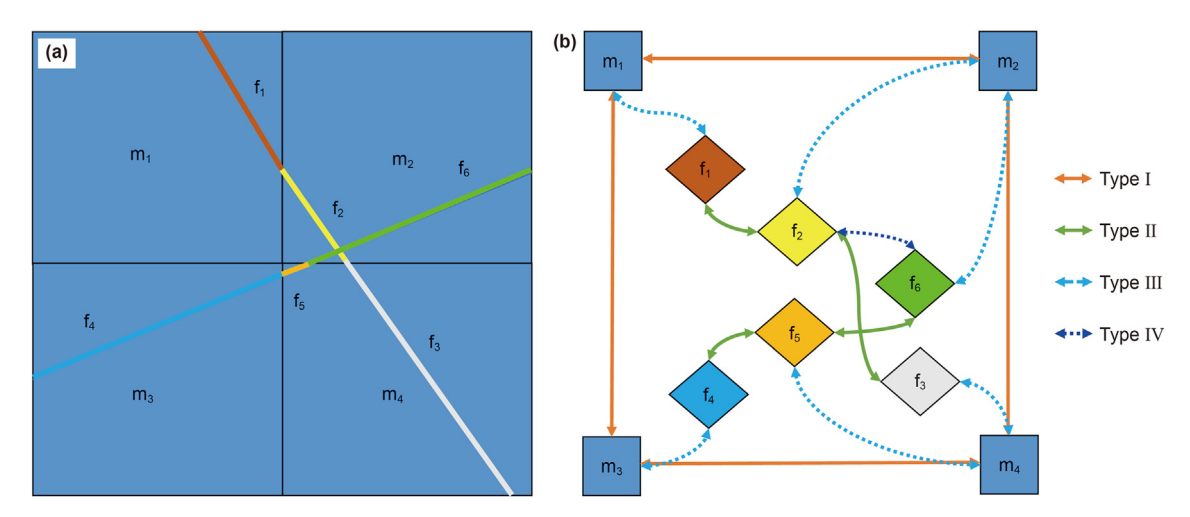


Fig. 7. Schematic of the model connection relationship: (a) schematic of grid blocks in the model; (b) schematic of the connection list.

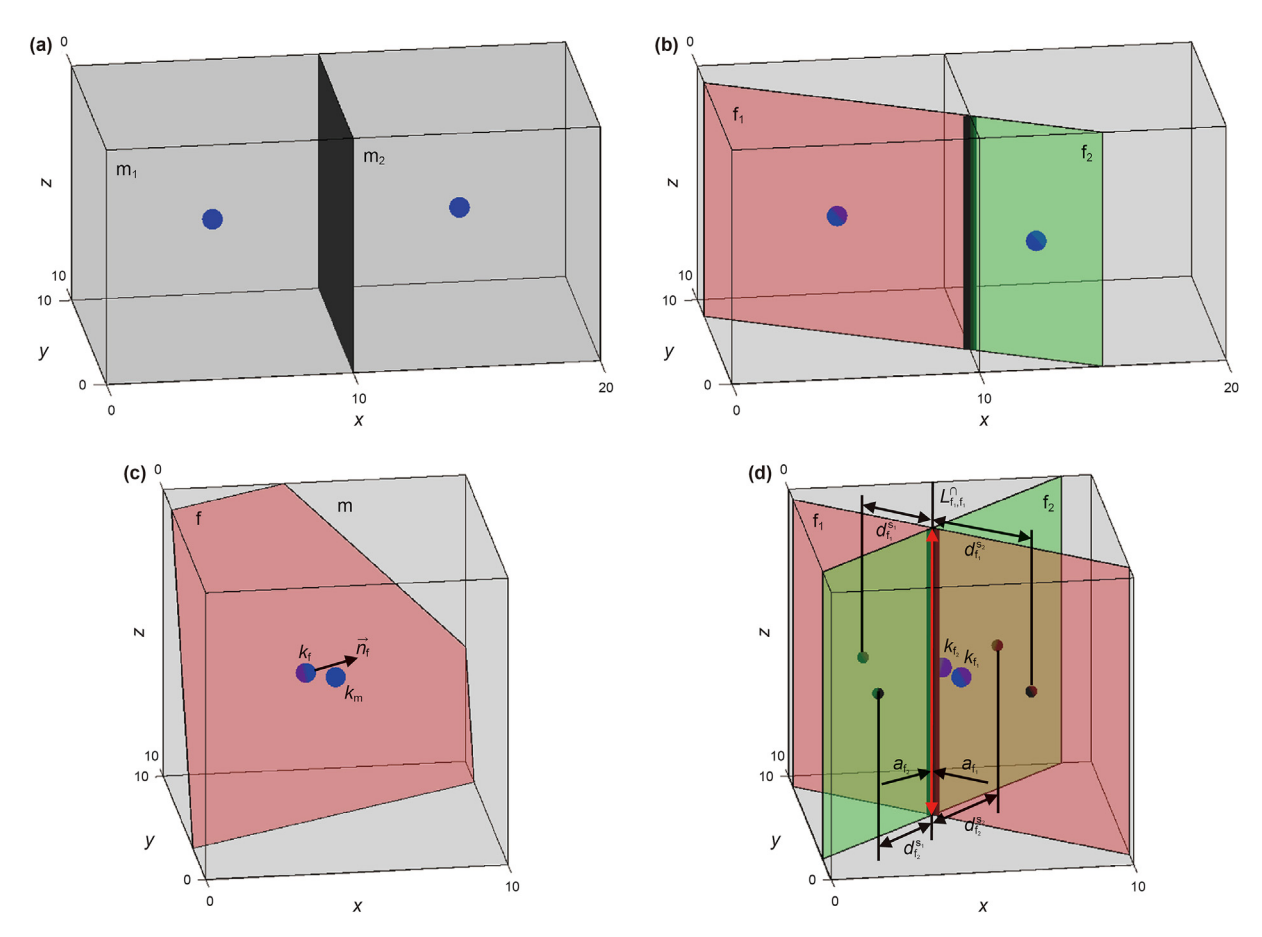


Fig. 8. Schematic of the parameters required for transmissibility calculation. (a) Type I; (b) Type II; (c) Type III; (d) Type IV.

applicable (Zolotukhin and Gayubov, 2021), as shown in Fig. 1(d). In such cases, the empirical Forchheimer equation can be used to characterize the post-Darcy (high-velocity non-Darcy) flow.

$$-\nabla\Phi = \frac{\mu}{\boldsymbol{k} \cdot \boldsymbol{k}_{r}} \boldsymbol{v} + \beta \rho \boldsymbol{v} |\boldsymbol{v}|$$
 (26)

For hydraulic fractures filled with proppants, Wu et al. (2014) obtained the correlation of β by matching with more than 180 data points.

$$\beta = 3.2808 \frac{1.485 \times 10^9}{\left(k_0 \times 10^{-15}\right)^{1.021}} \tag{27}$$

where β is the post-Darcy coefficient, \mathbf{m}^{-1} ; k_0 is the initial permeability, \mathbf{m}^2 .

Under multiphase flow conditions, the $f_{{\rm F},\alpha}^{{\rm Post-Darcy}}$ is expressed as follows:

$$f_{\mathrm{F},\alpha}^{\mathrm{Post-Darcy}} = \frac{2}{1 + \sqrt{1 + 4\rho_{\alpha}\beta \frac{k_{0}k_{r}}{u}|\boldsymbol{v}_{\alpha}|}}$$
(28)

In a low-permeability shale matrix, the oil phase typically exhibits pre-Darcy flow characteristics, as illustrated in Fig. 6. The boundary effect between rocks and fluids is generally considered the main factor leading to pre-Darcy flow, as shown in Fig. 1(e). In contrast, the water phase and gas phase obey Darcy flow (Wang et al., 2021). Prada and Civan (1999) assumed the matrix had a threshold pressure gradient (TPG) and used the piecewise function to describe the pre-Darcy flow phenomenon. However, recent studies have indicated that TPG may be 0 or very small to be ignored (Wang and Sheng, 2017). Therefore, Wang et al. (2020) proposed a continuous exponential function model to characterize the pre-Darcy (low-velocity non-Darcy) flow behavior. The $f_{\rm M,o}^{\rm Pre-Darcy}$ is defined as follows:

$$\begin{cases} f_{\text{M,o}}^{\text{Pre-Darcy}} = \left(\frac{1}{1 + ae^{-b|\nabla P_o|}}\right) \\ a = -0.6095 \left(\frac{k}{\mu_o}\right)^3 + 2.5821 \left(\frac{k}{\mu_o}\right)^2 - 3.4594 \frac{k}{\mu_o} + 1.5836 \\ b = 0.3603 \left(\frac{k}{\mu_o}\right)^2 - 0.1049 \frac{k}{\mu_o} + 1.0935 \end{cases}$$
(29)

where a and b are the experimental fitting coefficients; k is the permeability, mD; μ_0 is the viscosity of the oil phase, cP. This model guarantees that a curve passes through the origin. When the pressure gradient is sufficiently large or when a=0, Eq. (29) simplifies to the linear Darcy equation.

2.4.4. Stress sensitivity

For propped fractures, Alramahi and Sundberg (2012) conducted experiments to assess the influence of the normal effective stress (σ'_n) on fracture conductivity (C_f) under different stiffness shale proppant embedment conditions, as shown in Fig. 1(f). Wang and Fidelibus (2021) obtained the correlation between normalized fracture conductivity and closure pressure by analyzing and fitting their experimental data.

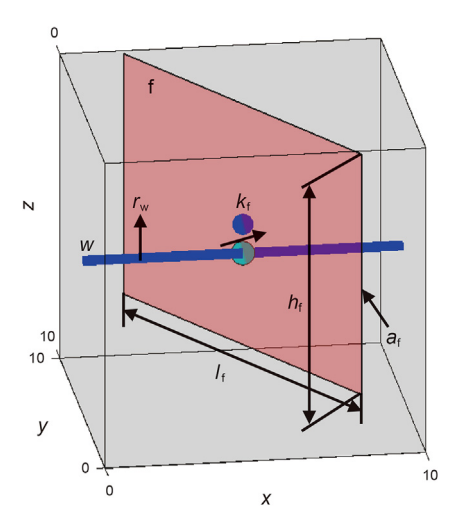


Fig. 9. Schematic of the parameters required for wellbore index calculation.

$$C_{\rm f} = 10^{c_1 \sigma_{\rm n}' + c_2} \tag{30}$$

where the units of $C_{\rm f}$ and $\sigma'_{\rm n}$ are mD·ft and psia, respectively; c_1 and c_2 are coefficients related to shale stiffness. For stiff shale, $c_1 = -0.00011$ and $c_2 = -0.0971$; for medium-stiff shale, $c_1 = -0.00035$ and $c_2 = 0.2396$; for soft shale, $c_1 = -0.00064$ and $c_2 = -0.4585$.

The propagation direction of a hydraulic fracture is normal to the minimum total horizontal stress $\sigma_{h,min}$. The total normal stress on the fracture can be approximated as the average total normal stress. Therefore, the σ_n' can be defined as

$$\sigma_{\rm n}' = \sigma_{\rm h,min} - \alpha_{\rm B}P \tag{31}$$

where α_B is the Biot constant.

A dynamical correction factor $f_{{\rm F},\alpha}^{\rm Stress}$ for hydraulic fracture is introduced

$$f_{F,\alpha}^{Stress} = \frac{C_f(P_\alpha)}{C_f(P_0)}$$
 (32)

For organic-rich source rocks with natural fractures, the stress sensitivity mechanism significantly differs from that of hydraulic fractures (Zhang and Emami-Meybodi, 2021). This study uses the Gangi model (see Fig. 1(g)) to describe the permeability variation with pressure (Wasaki and Akkutlu, 2015). The $f_{M,\alpha}^{\text{Stress}}$ is defined as

$$f_{\mathrm{M},\alpha}^{\mathrm{Stress}} = \frac{k_0}{k_{\mathrm{m}}} \left[1 - \left(\frac{\sigma_{\mathrm{c}} - \alpha_{\mathrm{B}} P}{E_{\mathrm{a}}} \right)^m \right]^3 \tag{33}$$

where k_0 is the matrix permeability under zero confining pressure; $k_{\rm m}$ is the initial matrix permeability; $\sigma_{\rm c}$ is the confining stress; $E_{\rm a}$ is the effective modulus of the rough body (the maximum effective stress of completely closed fracture); and m is a parameter related to roughness. Shi and Durucan (2016) proposed values of $E_{\rm a}$ and m for unconventional rock samples.

2.5. Embedded discrete fracture modeling

2.5.1. Transmissibility mathematical formulation

The EDFM can accurately capture the detailed geometry of each fracture and achieve accurate and efficient fracture modeling (Tene et al., 2017). The standard EDFM includes four types of connections: (1) adjacent matrix cells, (2) adjacent fracture cells within an individual fracture plane, (3) the connection between fracture cells and their corresponding host matrix cells, and (4) the connection between intersecting fracture cells from different fracture planes within the same matrix grid. Fig. 7 illustrates the relationships among these four connection types. The first two types are standard connections, as shown in Fig. 8(a) and (b). The latter two types are classified as non-neighboring connections (NNCs).

The two-point flux approximation (TPFA) is used to evaluate fluid flow between two cells (Olorode et al., 2020). The transmissibility for the first two types of standard connections is defined as

$$T_{ik} = \left[T_{i,k}^{-1} + T_{k,i}^{-1}\right]^{-1}, \ T_{i,k} = A_{i,k} k_i \frac{\boldsymbol{c}_{i,k} \cdot \boldsymbol{n}_{i,k}}{\left|\boldsymbol{c}_{i,k}\right|^2}$$
(34)

where T_{ik} is the face transmissibility; $T_{i,k}$ and $T_{k,i}$ are the half-transmissibility of the cell; $\mathbf{n}_{i,k}$ is the unit normal that points from the centroid of cell i to the face between cells i and k; $\mathbf{c}_{i,k}$ is the vector from the cell centroid to the face centroid.

More detailed information on the NNCs transmissibility in the

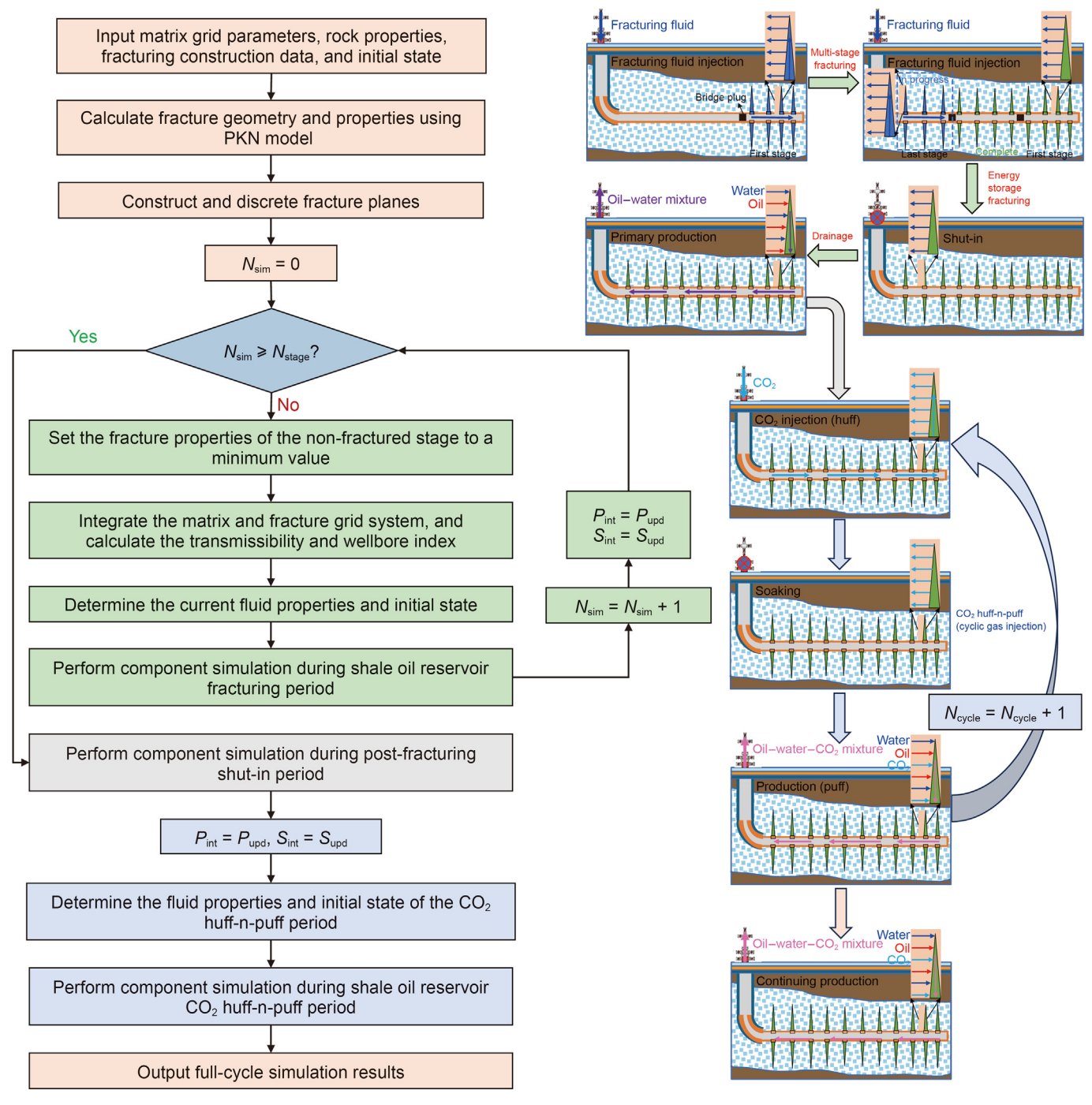


Fig. 10. Flow chart of life-cycle (fracturing, shut-in, production, CO₂ huff-n-puff) simulation.

Table 1Economic parameters (Jahangiri and Zhang, 2012).

Parameter	Value
Annual discount rate, %	10
CO ₂ injection cost, \$/t	60
Carbon tax credit, \$/t	40
Drilling cost (single well), \$	2.02×10^{6}
Oil price, \$/m ³	503.18
Water disposal cost, \$/m ³	6.29
Fracturing fluid cost, \$/m ³	132.09
Perforation cost (ten stages), \$	15.12×10^4

EDFM model can be referred to previous studies (Moinfar et al., 2014; Olorode et al., 2020). The NNCs transmissibility for both matrix-fracture connections and intersecting fracture connections are defined as follows:

$$T_{\mathrm{m,f}}^{\mathrm{nnc}} = \frac{k_{\mathrm{m,f}} \left(2A_{\mathrm{f}} \right)}{\int \left| \left(\boldsymbol{x} - \boldsymbol{x}_{\mathrm{ref}} \right) \cdot \boldsymbol{n}_{\mathrm{f}} \right| \mathrm{d}V / \int \mathrm{d}V}, \quad k_{\mathrm{m,f}} = \frac{\left(V_{\mathrm{m}} + V_{\mathrm{f}} \right)}{V_{\mathrm{m}} / k_{\mathrm{m}} + V_{\mathrm{f}} / k_{\mathrm{f}}}$$
(35)

Table 2 Model summary.

Model name	Grid type	Fracture model	Simulator
LGR-EFM	Local grid refinement	Explicit fracture model	E300
LGR-EDFM	Local grid refinement	Embedded discrete fracture model	MRST
CG-EDFM	Coarse grid	Embedded discrete fracture model	MRST

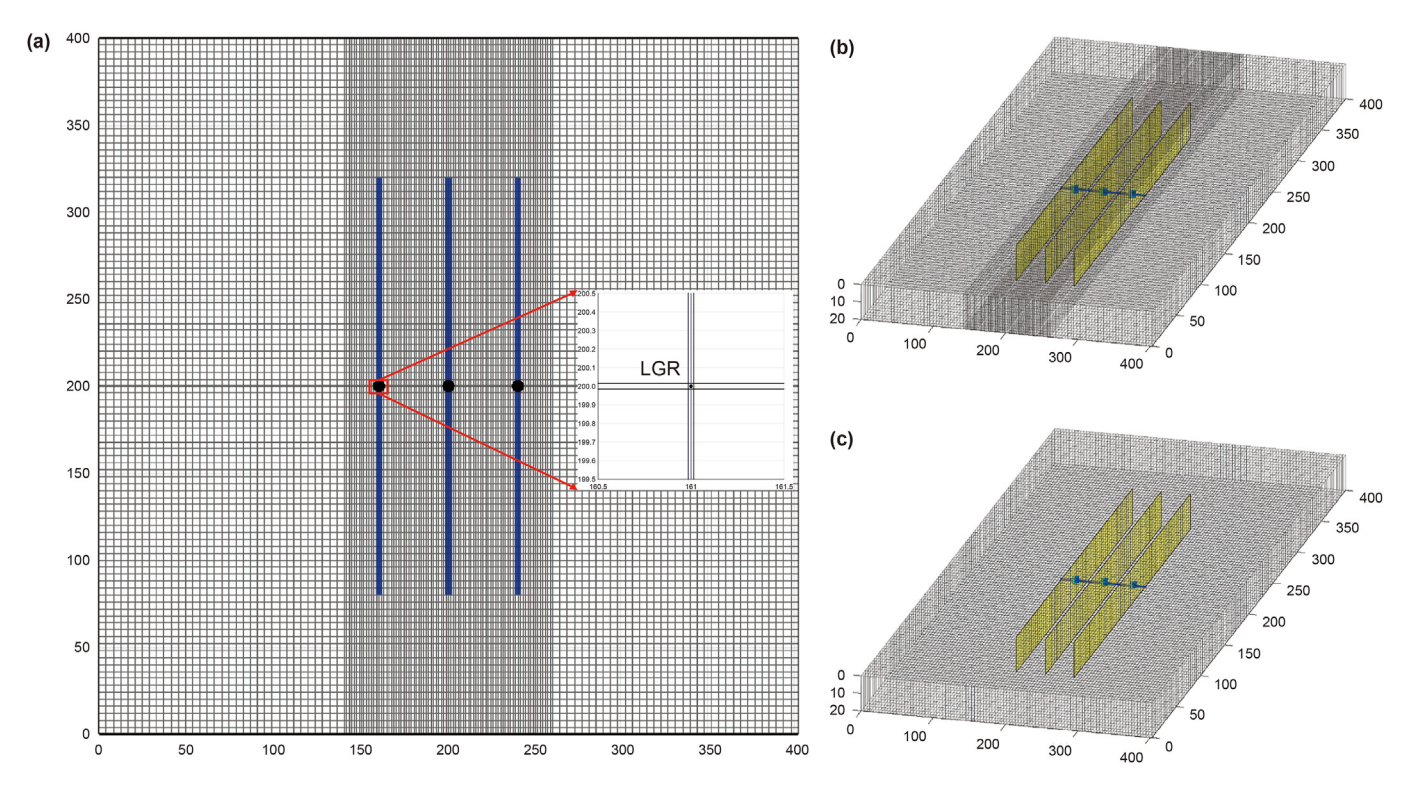


Fig. 11. Three types of reservoir grids: (a) LGR-EFM model; (b) LGR-EDFM model; (c) LGR-EDFM model.

Table 3Basic reservoir and fracture parameters.

Parameter	Value	Parameter	Value
Model dimension, m	$400\times400\times20$	Matrix permeability, μD	0.1
Matrix porosity, %	6.3	Fracture permeability, D	10
Fracture porosity, %	2	Fracture aperture, m	0.03
Initial pressure, MPa	32.405	Initial temperature, K	387.45
Water density, kg/m ³	1000	Water viscosity, cP	1
Water compressibility, MPa ⁻¹	8.5×10^{-4}	Rock compressibility, MPa ⁻¹	6.5×10^{-4}

Table 4 Compositional data for the EOS (Mallison et al., 2005).

Component	Molar fraction	Critical pressure, atm	Critical temperature, K	Critical volume, L/mol	Molar weight, g/mol	Acentric factor	Parachor coefficient
N ₂ /CH ₄	0.4630	45.2012	189.515	0.0997	16.1594	0.00854	77.00
CO_2	0.0164	72.9000	304.200	0.0926	44.0100	0.22800	78.00
$C_2 - C_5$	0.2052	40.4196	387.607	0.2171	45.5725	0.16733	155.50
$C_6 - C_{13}$	0.1911	33.0150	597.497	0.3812	117.7400	0.38609	367.40
$C_{14}-C_{24}$	0.1243	17.4525	698.515	0.7214	248.8270	0.80784	736.20

$$T_{f_{1},f_{2}}^{nnc} = \frac{T_{f_{1}}^{1/2}T_{f_{2}}^{1/2}}{T_{f_{1}}^{1/2} + T_{f_{2}}^{1/2}}, \quad \left(T_{f_{i}}^{1/2} = \frac{k_{f_{i}}a_{f_{i}}L_{f_{1},f_{2}}^{n}}{\left(d_{f_{i}}^{s_{1}} + d_{f_{i}}^{s_{2}}\right)/2}, \quad \forall i \in (1,2)\right)$$
(36)

where $k_{m,f}$ is the pore volume weighted harmonic average of

fracture and matrix permeabilities; A_f is the surface area of the fracture cell on one side; \mathbf{x} is the point in the matrix cell; \mathbf{x}_{ref} is any reference point on the fracture plane; and \mathbf{n}_f is the unit normal vector of the fracture plane. These parameters are illustrated in Fig. 8(c). $T_f^{1/2}$ is the fracture half-transmissibility; a_f is the fracture aperture; $L_{f1,f2}^{0}$ is the length of the intersection line between two fracture cells; and d_f^{s} is the normal distance from the center of the

 Table 5

 Binary interaction constants for oil components (Mallison et al., 2005).

Component	N ₂ /CH ₄	CO ₂	C ₂ -C ₅	C ₆ -C ₁₃	C ₁₄ -C ₂₄
N ₂ /CH ₄	0.11883	0.00071	0.000778	0.01	0.011
CO_2	0.00071	0.15	0.15	0.15	0.15
$C_2 - C_5$	0.000778	0.15	0	0	0
$C_6 - C_{13}$	0.01	0.15	0	0	0
C_{14} – C_{24}	0.011	0.15	0	0	0

fracture cell segment to the fracture intersection point. These parameters are illustrated in Fig. 8(d).

2.5.2. Wellbore effect

In the EDFM model, when a fracture segment intersects with a wellbore trajectory, the control volume representing the fracture segment should be regarded as a well block. Moinfar et al. (2014) modified the classic Peaceman model to calculate the effective wellbore index (*WI*) for fractured horizontal wells.

$$\begin{split} WI &= \frac{2\pi k_f a_f}{\ln(r_e/r_{w\theta}) + S}, \quad r_{w\theta} = r_w \frac{1 + \sin(\theta)}{2\sin(\theta)}, \\ r_e &= 0.14 \sqrt{\left(l_f\right)^2 + \left(h_f\right)^2} \end{split} \tag{37}$$

where $k_{\rm f}$ is the fracture permeability; θ is the angle between the wellbore axis and the fracture plane; $r_{\rm e}$ and $r_{\rm w}\theta$ are the equivalent wellbore and actual wellbore radius, respectively; S is the surface factor, dimensionless; $l_{\rm f}$ and $h_{\rm f}$ are the length and height of the fracture segment, respectively. The parameters are illustrated in Fig. 9.

2.6. Discretization and solution of governing equation

2.6.1. Numerical solution

To numerically solve Eqs. (1) and (2), the backward Euler scheme is first used for temporal discretization. The semi-discrete form of Eqs. (1) and (2) can be written as

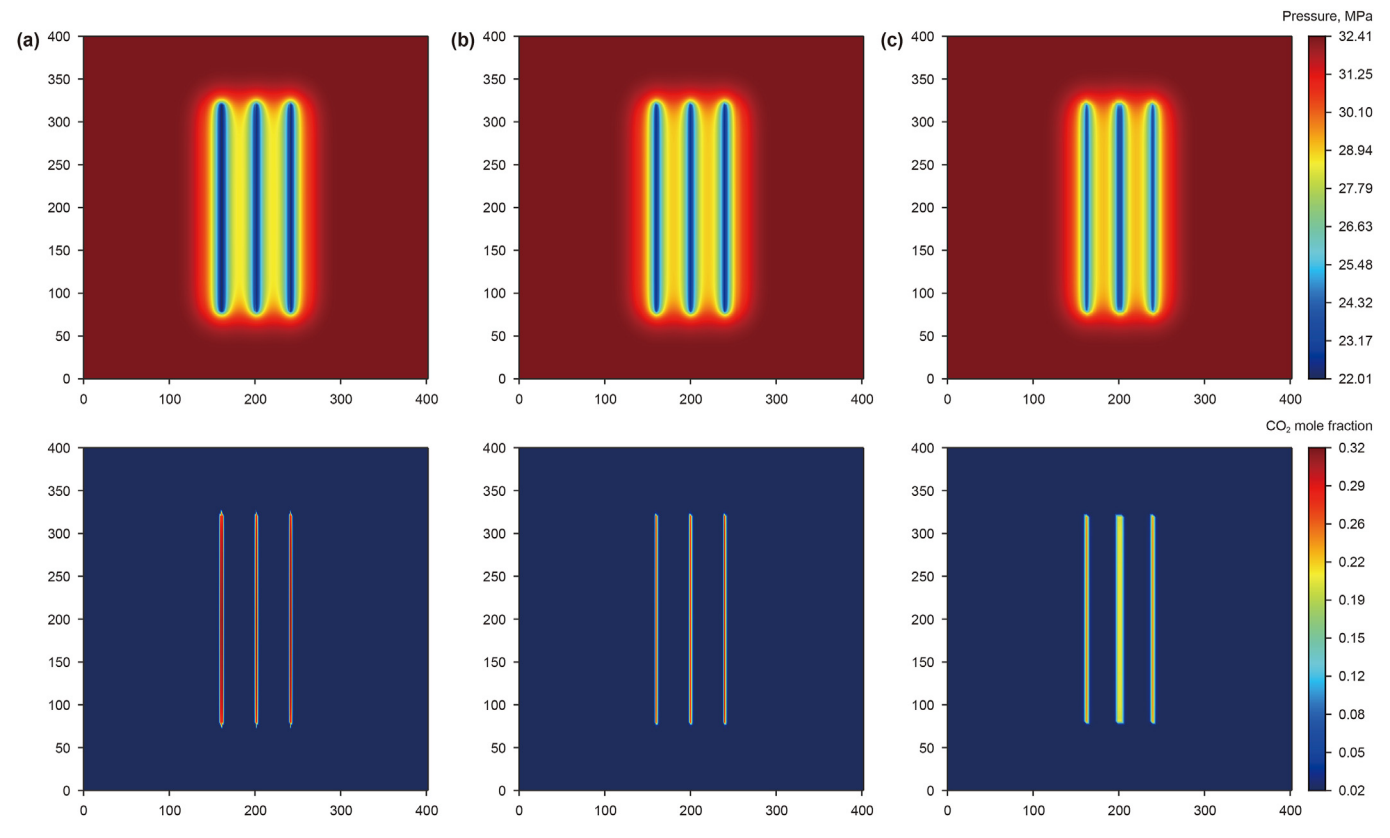


Fig. 12. The pressure (top) and CO₂ mole fraction (bottom) distributions of the three models at the end of huff-n-puff: (a) LGR-EFM model; (b) LGR-EDFM model; (c) LGR-EDFM model.

Table 6Comparison of production and numerical solution of three models.

Parameter	LGR-EFM	LGR-EDFM	CG-EDFM
Initial oil production rate, m³/day	47.16	18.80	7.88
Cumulative oil production in the primary period, m ³	871.42	828.51	778.34
Total oil production, m ³	1229.69	1200.93	1142.52
Total wall time, min	31.20	48.86	15.29
Total number of iterations	278	580	265

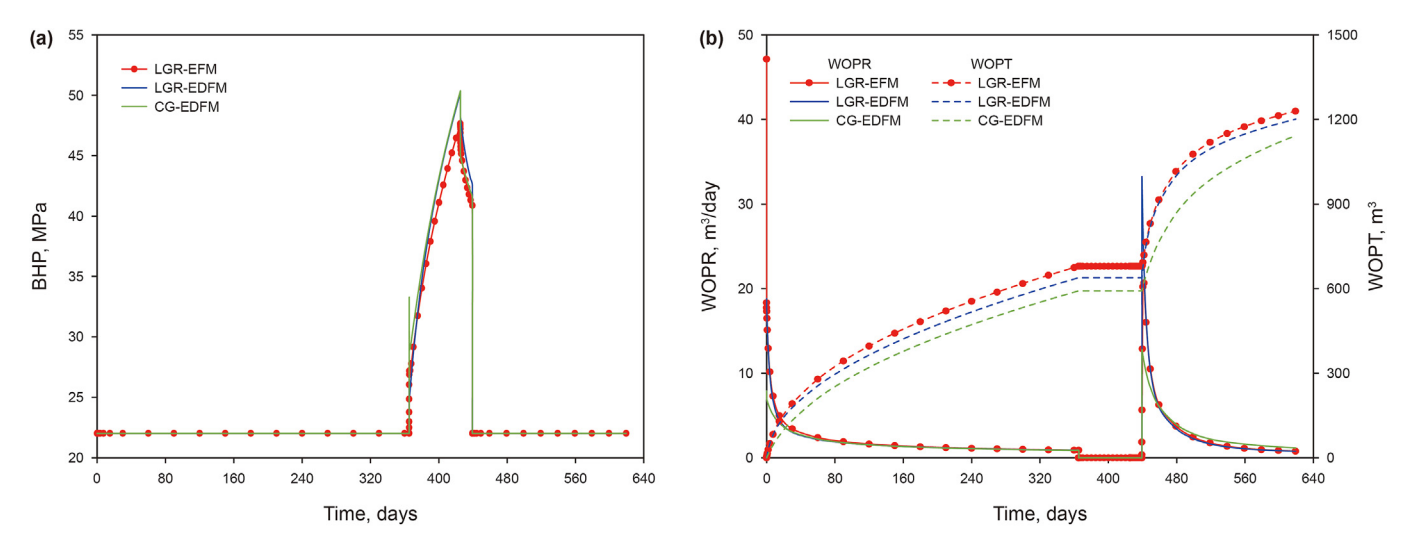


Fig. 13. BHP (a) and well oil production rate (WOPR) (b) curves of three models.

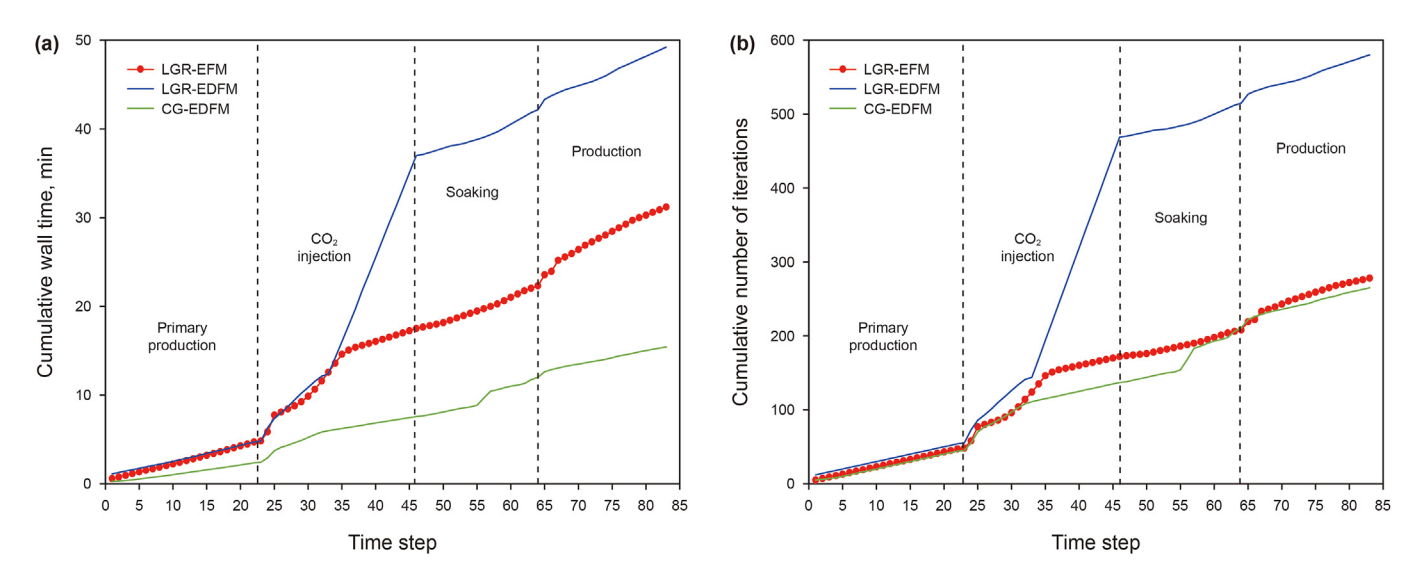


Fig. 14. The cumulative wall time (a) and iteration number (b) curves of three models.

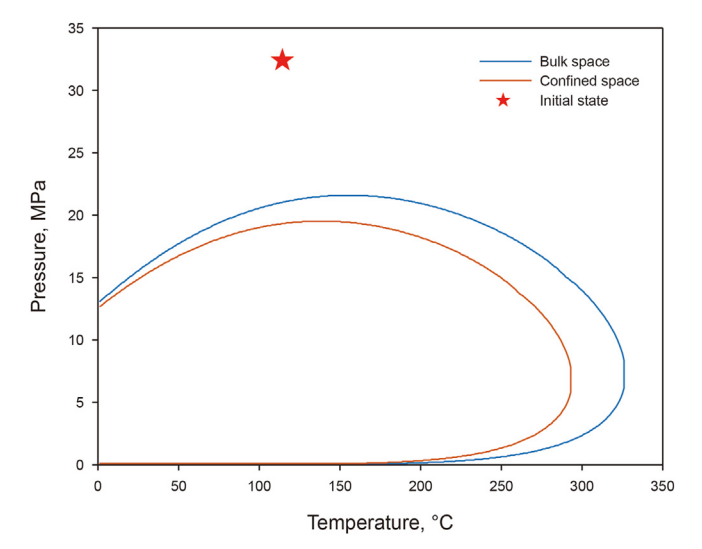


Fig. 15. Phase envelope of the mixture in confined and bulk space.

$$\frac{1}{\Delta t} \left[\left(\phi \rho_{L} S_{L} X_{L}^{i} + \phi \rho_{V} S_{V} X_{V}^{i} \right)^{n+1} - \left(\phi \rho_{L} S_{L} X_{L}^{i} + \phi \rho_{V} S_{V} X_{V}^{i} \right)^{n} \right]
+ \nabla \cdot \left(\rho_{L} X_{L}^{i} \boldsymbol{v}_{L} + \rho_{V} X_{V}^{i} \boldsymbol{v}_{V} + J_{L}^{i} + J_{V}^{i} \right) - \left(\rho_{L} X_{L}^{i} q_{L}^{\text{well}} + \rho_{V} X_{V}^{i} q_{V}^{\text{well}} \right) \right/ V + \left(\rho_{L} X_{L}^{i} q_{L}^{\text{nnc}} + \rho_{V} X_{V}^{i} q_{V}^{\text{nnc}} \right) / V = R_{i}$$
(38)

$$\frac{1}{\Delta t} \left[(\phi \rho_{\mathsf{w}} S_{\mathsf{w}})^{n+1} - (\phi \rho_{\mathsf{w}} S_{\mathsf{w}})^{n} \right] + \nabla \cdot (\rho_{\mathsf{w}} \boldsymbol{v}_{\mathsf{w}}) \\
- \rho_{\mathsf{w}} \left(q_{\mathsf{w}}^{\mathsf{well}} - q_{\mathsf{w}}^{\mathsf{nnc}} \right) / V = R_{\mathsf{w}}$$
(39)

where n+1 denotes the next time step, and n denotes the current time step. All other terms without these superscripts are calculated at the current time step. $q^{\rm nnc}$ is the total flow flux between NNCs; and $q^{\rm well}$ is the source term of the well.

The finite volume method (FVM) with TPFA is used to discretize flux terms, including both advection and diffusion terms.

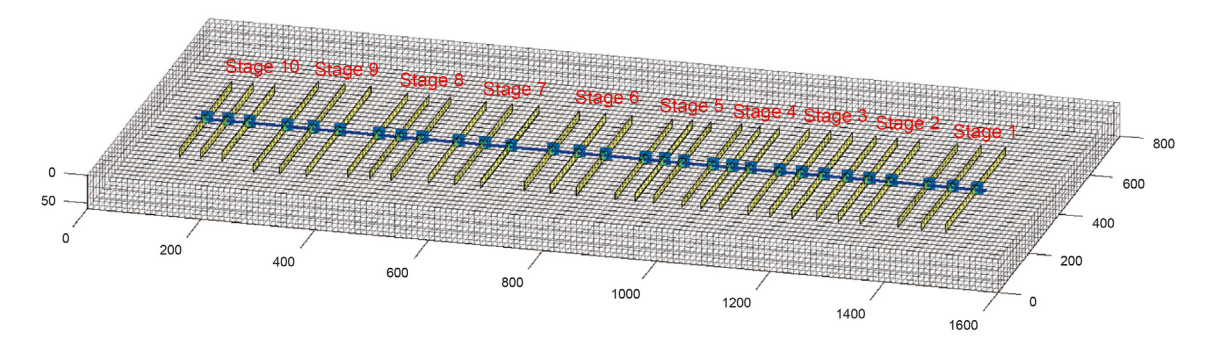


Fig. 16. Physical model of shale oil reservoirs.

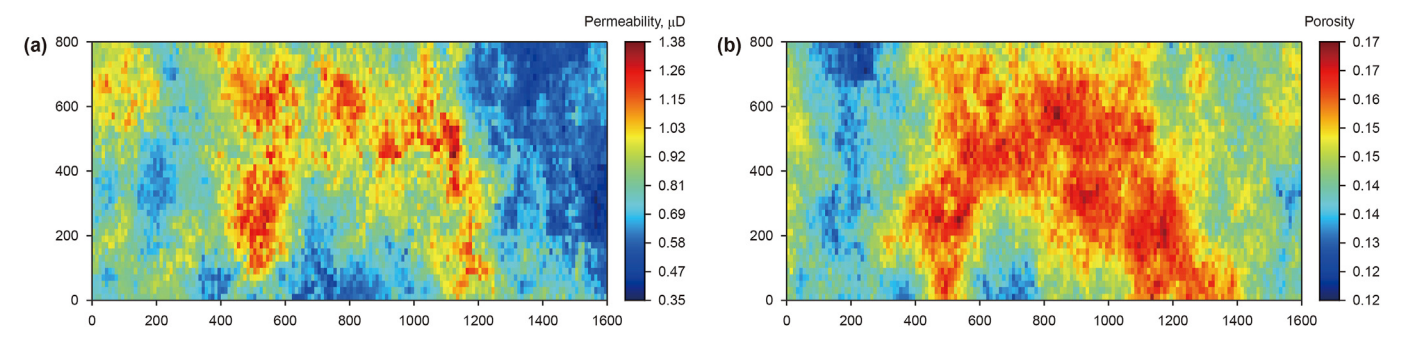


Fig. 17. The matrix permeability (**a**) and porosity (**b**) distribution of the second layer.

Table 7Basic reservoir and production parameters.

Parameter	Value	Parameter	Value
Model dimension, m	1600 × 800 × 60	Number of grid blocks	160 × 40 × 3
Fracture permeability, D	40.87	Fracture porosity	0.02
Fracture aperture, m	0.03	Number of stages	10
Clusters per stage	3	Initial water saturation	0.17
Initial pressure, MPa	32.405	Initial temperature, K	387.45
Water density, kg/m ³	1000	Water viscosity, cP	1
Water compressibility, MPa ⁻¹	8.5×10^{-4}	Rock compressibility, MPa ⁻¹	6.5×10^{-4}
Minimum horizontal stress, MPa	65	Biot constant	1
Confining stress, MPa	68.94	Effective modulus, MPa	96.52
Bulk shear modulus, GPa	10.41	Drained Poisson's ratio	0.2
Fracturing fluid viscosity, cP	1	Leak-off coefficient, m/min ^{0.5}	5.42×10^{-3}

Additionally, discrete operators are introduced to simulate the continuous counterparts of the divergence and gradient operators (Lie, 2019). The fully discrete forms of Eqs. (38) and (39) can be written as

$$\begin{split} & \frac{V}{\Delta t} \left[\left(\phi \rho_{L} S_{L} X_{L}^{i} + \phi \rho_{V} S_{V} X_{V}^{i} \right)^{n+1} - \left(\phi \rho_{L} S_{L} X_{L}^{i} + \phi \rho_{V} S_{V} X_{V}^{i} \right)^{n} \right] \\ & + \operatorname{div} \left(\rho_{L} X_{L}^{i} \boldsymbol{v}_{L} + \rho_{V} X_{V}^{i} \boldsymbol{v}_{V} + J_{L}^{i} + J_{V}^{i} \right)^{n+1} \\ & - \left(\rho_{L} X_{L}^{i} q_{L}^{\text{well}} + \rho_{V} X_{V}^{i} q_{V}^{\text{well}} \right)^{n+1} + \left(\rho_{L} X_{L}^{i} q_{L}^{\text{nnc}} + \rho_{V} X_{V}^{i} q_{V}^{\text{nnc}} \right)^{n+1} \\ & = R_{i}^{n+1} \end{split}$$

$$(40)$$

 $\frac{V}{\Delta t} \left[(\phi \rho_{\mathsf{w}} S_{\mathsf{w}})^{n+1} - (\phi \rho_{\mathsf{w}} S_{\mathsf{w}})^{n} \right] + \operatorname{div}(\rho_{\mathsf{w}} \boldsymbol{v}_{\mathsf{w}})^{n+1} \\
- \left(\rho_{\mathsf{w}} q_{\mathsf{w}}^{\mathsf{well}} - \rho_{\mathsf{w}} q_{\mathsf{w}}^{\mathsf{nnc}} \right)^{n+1} = R_{\mathsf{w}}^{n+1}$ (41)

$$\mathbf{v}_{\alpha} = -T_{ik}\lambda_{\alpha}^{n+1}\left[\operatorname{grad}\left(P_{\alpha}^{n+1}\right) - \rho_{\alpha}^{n+1}\operatorname{ggrad}(z)\right]$$
 (42)

$$q_{\alpha}^{nnc} = \sum_{m=1}^{N_{nnc}} T_{m}^{nnc} \lambda_{\alpha}^{n+1} \left[(P_{\alpha} - \rho_{\alpha} gz) - (P_{\alpha} - \rho_{\alpha} gz)_{m}^{nnc} \right]$$
(43)

$$q_{\alpha}^{\text{well}} = WI\lambda_{\alpha}^{n+1}(P_{e} - P_{b}) \tag{44}$$

where symbols div and grad in Eqs. (40) and (42) are the discrete divergence and gradient operators, respectively; subscript m denotes the index from 1 to $N_{\rm nnc}$; $N_{\rm nnc}$ is the total number of NNCs for each cell; $P_{\rm b}$ is the bottom-hole pressure; and $P_{\rm e}$ is the pore pressure at the equivalent wellbore radius. The transmissibility can be seen from Eqs. (34)–(36).

The temporal and spatial discretization schemes can lead to the mass imbalance, referred to as the residual (R). The MRST automatic differential (AD) technique is used to calculate the partial derivatives of the residuals (R) for each primary variable (i.e., Jacobian

 Table 8

 Basic operating parameters in the development stage.

Parameter	Value	Parameter	Value
Production bottom-hole pressure, MPa	23.01	Primary production time, years	5
CO ₂ injection rate, m ³ /s	3.28	Maximum bottom-hole pressure, MPa	62.405
CO ₂ injection time, days	60	Soaking time, days	14
Production time, days	180	Number of cycles	5
Continuing production time, years	5	Total simulation time, days	4922

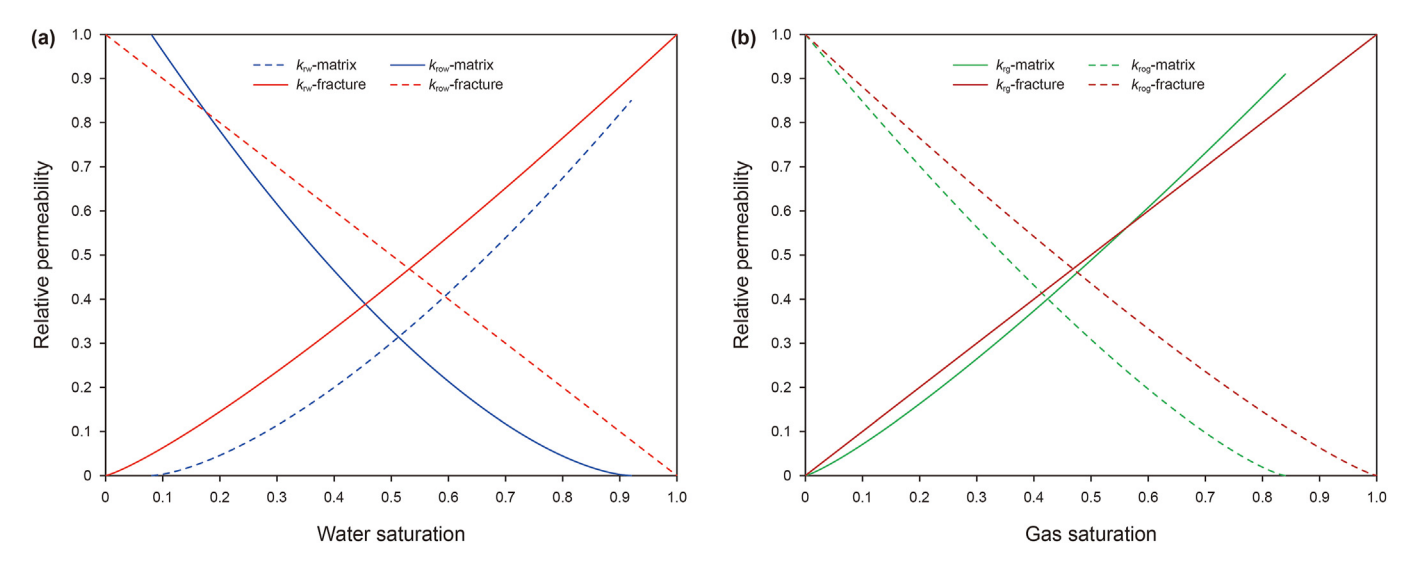


Fig. 18. The water-oil (a) and oil-gas (b) relative permeability curves.

matrix). Various options exist for choosing primary variables (Voskov and Tchelepi, 2012). This study uses a natural variable composition formulation to couple flow and thermodynamics. For each grid, the primary variables include pressure (p), liquid phase saturation (S_L) , and phase composition of each component $(x_1, ..., x_{N_{c-1}})$ and $y_1, ..., y_{N_{c-1}}$). Before linearizing the system, these $2N_c$ primary variables are paired with N_c mass conservation and N_c isofugacity equations.

Furthermore, the Schur-complement procedure is used to express the mass conservation equations as functions of the primary variables only. The Newton—Raphson method is applied by performing the Taylor expansion on the residual at the current timestep and the current Newton iteration, expressed as

$$\frac{\partial \mathbf{R}}{\partial \mathbf{x}} \delta \mathbf{x}^{i+1} = -\mathbf{R} \left(\mathbf{x}^{i} \right), \ \mathbf{x}^{i+1} \leftarrow \mathbf{x}^{i} + \delta \mathbf{x}^{i+1}$$

$$\tag{45}$$

where i is the number of nonlinear iterations. This study combines the bi-conjugate gradient-stabilized linear solver with the algebraic multigrid (AMG) (Demidov, 2019). Subsequently, the change in the primary variables is added to its previous value, and this process is repeated until the system converges. The program will repeat this process to complete the numerical solution for the next time step.

2.6.2. Life-cycle solution workflow

The life-cycle process of the shale oil reservoirs in this work includes five periods: the fracturing period, the shut-in period, the primary depletion production period, the CO_2 huff-n-puff period, and the continuing depletion production period. The seepage field at the end of the previous period is taken as the initial value of the next period. Fig. 10 illustrates the life-cycle simulation flow chart. $N_{\rm sim}$ and $N_{\rm stage}$ are the number of completed fracturing stages and

the total number of stages, respectively. $P_{\rm int}$ and $P_{\rm upd}$ are the pressure of the previous and current time steps, respectively. $S_{\rm int}$ and $S_{\rm upd}$ are the saturation of the previous and current time steps, respectively.

2.7. CCUS-EOR evaluation

2.7.1. Net present value

The oil production or recovery factor is an essential index for evaluating the performance of EOR technology. This study further conducted an economic analysis of the life-cycle process to evaluate the economic feasibility of shale oil reservoir fracturing and development. This evaluation provides a basis for collaborative optimization of hydraulic fracturing, CO₂ flooding, and CO₂ storage. The total value of a potential investment can be expressed by net present value (NPV). The NPV of a single well is defined as follows:

present value (NPV). The NPV of a single well is defined as follows:
$$\begin{cases} \text{NPV} = \sum_{t=1}^{T_{\text{CU}}} \frac{C_t}{(1+r)^{t/365}} - C_f - C_p - C_d \\ C_t = r_0 \times Q_{0,p}^t - r_{\text{CO}_2,i} \times Q_{\text{CO}_2,i}^t - r_{\text{w,re}} \times Q_{\text{w,p}}^t + \text{TAX}_{\text{CO}_2} \times Q_{\text{CO}_2,s}^t \\ C_f = r_f \times Q_{f,i}^t \end{cases} \tag{46}$$

where T_{cu} , t, C_{t} , r, C_{f} , C_{p} , and C_{d} are the cumulative time, time step, annual cash inflow, annual discount rate, fracturing cost, perforation cost, and drilling cost, respectively; $Q_{0,p}^t$, $Q_{\text{CO}_2,i}^t$, $Q_{\text{w,p}}^t$, $Q_{\text{CO}_2,s}^t$, and $Q_{f,i}^t$ are the cumulative oil production, cumulative CO_2 purchase and injection, cumulative water production, cumulative CO_2 storage, and cumulative fracturing fluid injection, respectively; r_0 , $r_{\text{CO}_2,i}$,

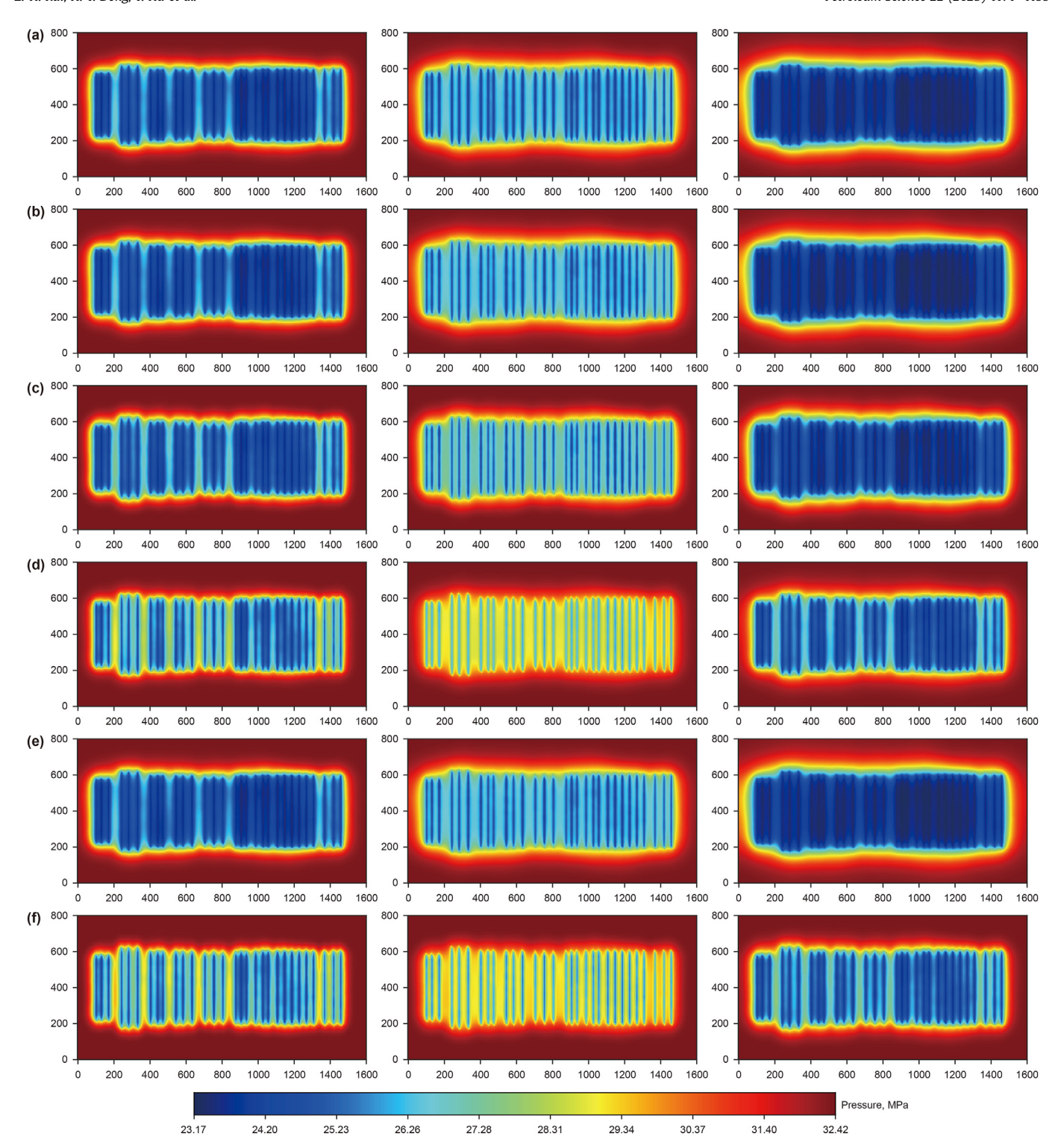


Fig. 19. The second layer pressure distribution under different mechanisms at the end of the primary production (left), the end of the five CO_2 cycles (middle), and the end of the simulation (right). (a) Confinement effect; (b) molecular diffusion; (c) pre-/post-Darcy flow; (d) stress sensitivity; (e) no-mechanism; (f) multi-mechanism.

 $r_{\rm W,re}$, TAX_{CO2}, and $r_{\rm f}$ represent oil price per m³, CO₂ injection cost per ton (including purchase, transportation, and injection), water disposal cost per m³, tax credit of CO₂ stored per ton, and fracturing fluid cost per m³. The NPV is calculated using the economic parameters provided in Table 1.

2.7.2. CO₂ utilization and storage factor

The CO₂ utilization and storage performance are essential indexes for CCUS-EOR. The CO₂ utilization factor (UF) and the CO₂ storage factor (SF) are important parameters to quantitatively evaluate the CO₂-EOR and geological storage capacity (Wang et al., 2024). The UF is the ratio of oil production volume to CO₂ injected mass during the huff-n-puff period at the surface condition. The UF

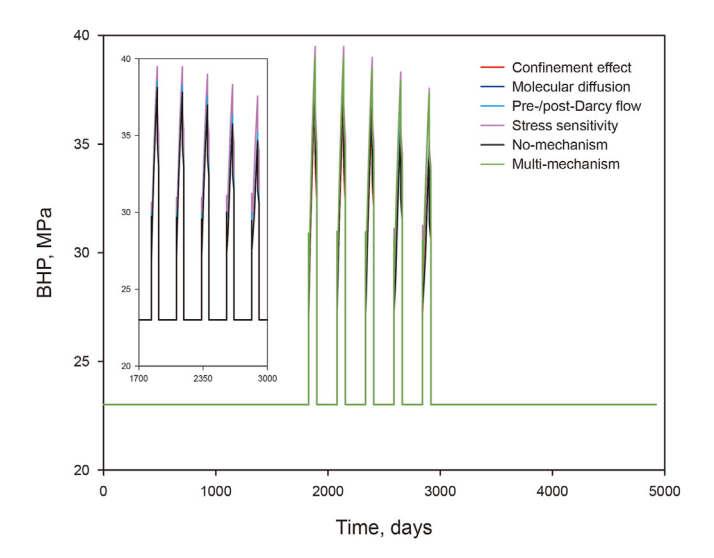


Fig. 20. The effect of different mechanisms on BHP.

indicates the oil displacement efficiency of CO₂. The SF is defined as the ratio of CO₂ captured by the formation to the mass of CO₂ injected. The SF reflects the storage capacity of CO₂.

$$UF = P_{V,Oil}^{SC} / I_{m,CO_2}^{SC}$$

$$(47)$$

$$SF = \left(I_{m,CO_2}^{RC} - P_{m,CO_2}^{RC}\right) / I_{m,CO_2}^{RC}$$
(48)

where superscripts RC and SC denote the reservoir and surface conditions, respectively; $P_{V,Oil}$ is the cumulative oil production volume after CO₂ injection, m³; I_{m,CO_2} is the cumulative injected CO₂ mass, t; P_{m,CO_2} is the cumulative produced CO₂ mass after CO₂ gas injection, t.

3. Model validation and mechanism analysis

3.1. Model validation

Based on the validation method by Olorode et al. (2020), this

of 22.01 MPa. Therefore, each cycle of huff-n-puff lasts 254 days, and the total simulation time is 619.24 days. Fig. 12 shows the three models' pressure and CO₂ mole fraction distributions. The results indicate that the pressure and CO₂ mole fraction distributions in the LGR-EDFM model closely resemble those in the LGR-EFM model. Furthermore, the pressure distribution of the CG-EDFM model is similar to that of the LGR-EFM. Table 6 summarizes the production and simulation process information of the three models. Fig. 13 illustrates the changes in BHP and production during primary production and CO₂ huff-n-puff. From Fig. 13, it is evident that the BHP and WOPR of the LGR-CO2 mole fraction 800 0.551 0.492 0.254 0 195 0 135 0.076 400 600 800 1200 1400 1000 1600

study uses ECLIPSE 300 (E300) and MRST for model validation. E300 is a commercial simulator, and MRST is an open-source

simulation software. They can perform fully implicit component

simulation. The accuracy of MRST in component simulation has

been extensively validated (Lie and Møyner, 2021). This study es-

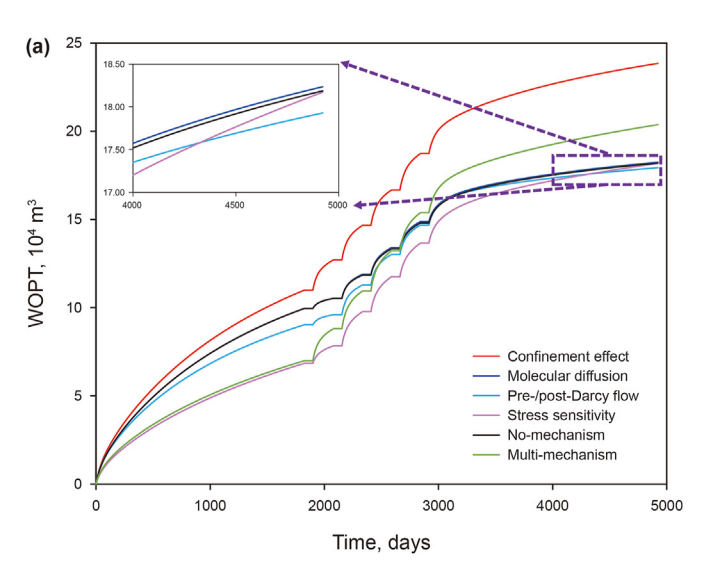
tablishes three models to validate the accuracy of the numerical solution, as shown in Table 2. Fig. 11 illustrates the grid structures of

the different models. Table 3 provides the basic reservoir and

fracture parameters. Table 4 is the properties of shale oil pseudocomponents, and Table 5 is their binary interaction constants. Primary production is conducted for one year with a fixed bottom-hole pressure (BHP) of 22.01 MPa. Subsequently, the CO₂

huff-n-puff technique is applied. The CO_2 injection rate is 0.082 m³/s, with a maximum BHP of 62.405 MPa. Following 60 days of CO_2 injection, the horizontal well is shut in and soaked for 14 days. Then, the well is put back into production for 180 days with a BHP

Fig. 22. The distribution of CO_2 mole fraction in the second layer of the molecular diffusion model at the end of five cycles.



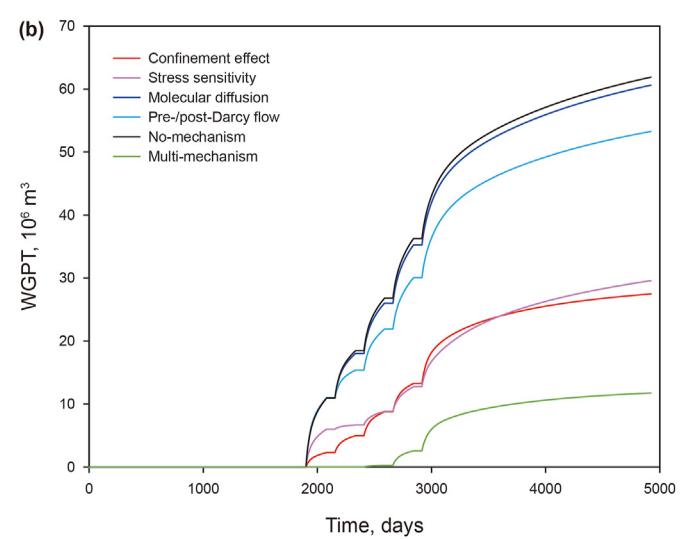


Fig. 21. The effect of different mechanisms on WOPT (a) and WGPT (b).

Table 9The effect of different mechanisms on production, NPV, UF, and SF.

Mechanism	WOPT, 10 ⁴ m ³	WGPT, 10 ⁶ m ³	NPV, 10 ⁶ \$	UF, m ³ /t	SF, t/t
Confinement effect	23.85	27.49	67.66	1.40	0.57
Molecular diffusion	18.23	60.62	57.75	0.90	0.58
Pre-/post-Darcy flow	17.93	53.27	50.86	0.97	0.57
Stress sensitivity	18.17	29.59	46.93	1.23	0.59
No-mechanism (base)	18.19	61.90	52.60	0.89	0.56
Multi-mechanism	20.37	11.75	52.75	1.45	0.61

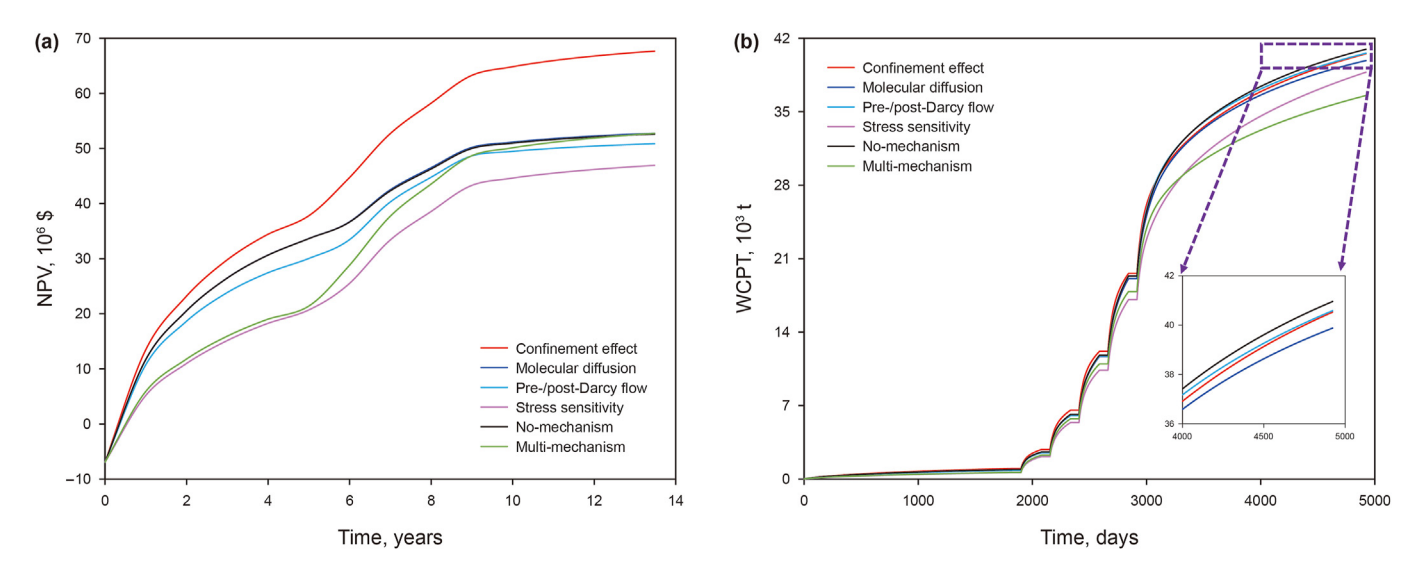


Fig. 23. The effect of different mechanisms on NPV (a) and WCPT (b).

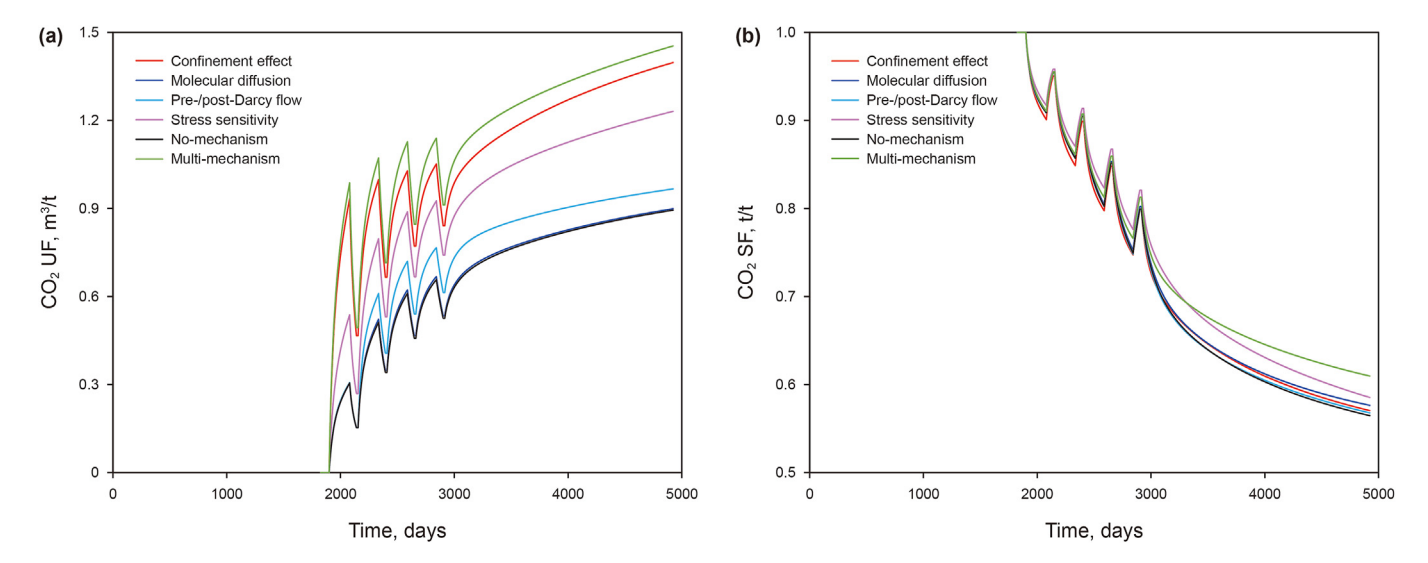


Fig. 24. The effect of different mechanisms on CO_2 UF (a) and CO_2 SF (b).

EDFM model closely align with those of the LGR-EFM model, demonstrating good consistency. For the CG-EDFM model, the average error in BHP is 7.26% compared to the LGR-EFM model, with a production error of 7.09%. Despite slightly reducing simulation accuracy, the CG-EDFM model is still reliable.

Table 6 and Fig. 14 indicate that increasing grid resolution can more accurately capture the initial oil production rate. However, this also increases computing costs and generates potential convergence issues. The CG-EDFM model reduces wall time and

number of iterations by 68.71% and 54.31%, respectively, compared to the LGR-EDFM model. Therefore, considering both simulation accuracy and efficiency, the CG-EDFM model is selected for subsequent mechanism and sensitivity analyses.

3.2. Mechanism analysis

A series of models are constructed and analyzed to evaluate the effects of various mechanisms on CCUS-EOR. The models include a

Table 10The parameters of fracture height, fracture length, displacement, and fluid volume.

Stage number Height, m		ight, m Displacement, m ³ /min	Fracturing fluid volume, m ³		Dimensionless time			Fracture length, m			
			Case 1	Case 2	Case 3	Case 1	Case 2	Case 3	Case 1	Case 2	Case 3
Stage 1	14.5	20.9	3129.9	3629.9	4129.9	0.013	0.016	0.020	348.7	392.6	435.3
Stage 2	15.5	20.1	3283.8	3783.8	4283.8	0.017	0.021	0.026	346.2	387.8	428.2
Stage 3	16.0	20.3	3552.4	4052.4	4552.4	0.019	0.024	0.028	358.7	398.6	437.4
Stage 4	13.0	20.9	2729.3	3229.3	3729.3	0.001	0.012	0.015	341.0	390.1	437.8
Stage 5	14.0	21.0	2840.0	3340.0	3840.0	0.011	0.014	0.017	331.5	377.4	421.9
Stage 6	16.0	20.8	3170.6	3670.6	4170.6	0.015	0.019	0.023	325.9	366.4	405.9
Stage 7	14.5	20.9	2983.0	3483.0	3983.0	0.012	0.015	0.019	335.5	379.8	422.8
Stage 8	14.0	20.9	2976.1	3476.1	3976.1	0.012	0.015	0.018	344.4	390.0	434.3
Stage 9	14.0	21.1	3387.9	3887.9	4387.9	0.014	0.017	0.020	381.3	425.7	469.0
Stage 10	16.0	21.0	2932.9	3432.9	3932.9	0.013	0.016	0.020	305.6	346.7	386.5

no-mechanism model (basic model), four kinds of single-factor mechanism models (considering nano-confinement effect, molecular diffusion, pre-/post-Darcy flow, and stress sensitivity), and a multi-mechanism model. The methodology in this section is similar to the conventional CO₂ huff-n-puff simulation (i.e., excluding the fracturing and shut-in periods). The fluid parameters in these models are consistent with those in the previous section. Fig. 15 illustrates the phase envelopes of the initial components in both confined and bulk spaces. The nano-confinement effect causes the phase envelope to shrink inward and decrease the bubble point pressure ([ia et al., 2023).

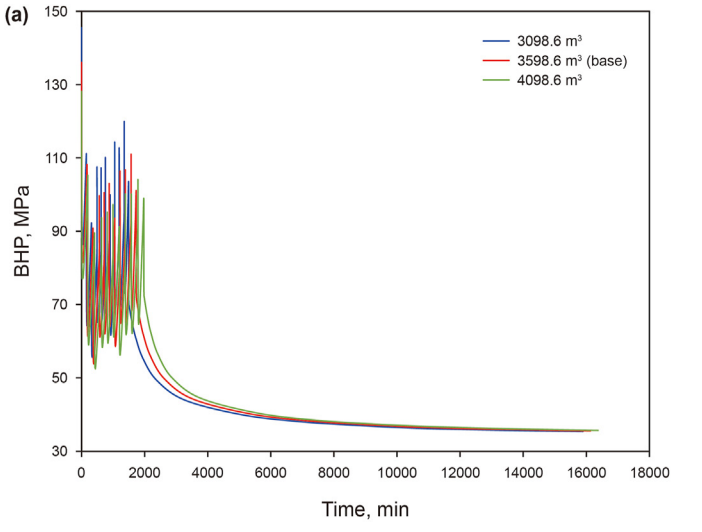
The reservoir model has dimensions of 1600 m \times 800 m \times 60 m and consists of three layers. The unequal height hydraulic fractures are located in the middle layer, as depicted in Fig. 16. The permeability and porosity of the first layer range from 0.08 to 1.05 μ D and 0.08 to 0.16, respectively. For the third layer, the permeability and porosity range from 0.08 to 1.13 μ D and 0.08 to 0.16, respectively. The permeability and porosity of the second layer are illustrated in Fig. 17. Table 7 presents the basic parameters of the reservoir. Table 8 lists the basic operating parameters of these models. Based on the dual-medium theory, this study uses the Corey model to characterize the water-wet fractures and mixed-wetting matrix (Agada et al., 2016). The relative permeability curves for the matrix and fractures are shown in Fig. 18. According to Lie (2019), the relative permeability of the oil phase is defined as follows:

$$k_{\rm ro}(S_{\rm g}, S_{\rm w}) = \frac{S_{\rm g}k_{\rm rog}(S_{\rm o})}{S_{\rm g} + S_{\rm w} - S_{\rm wc}} + \frac{(S_{\rm w} - S_{\rm wc})k_{\rm row}(S_{\rm o})}{S_{\rm g} + S_{\rm w} - S_{\rm wc}}$$
(49)

where k_{rog} is the relative permeability of the oil phase in the oil—gas system; k_{row} is the relative permeability of the oil phase in the oil—water system.

Fig. 19 illustrates the pressure distribution for each model at the end of primary production, the end of the CO₂ huff-n-puff cycle, and the end of the simulation. According to the results, the formation pressure at the end of the huff-n-puff cycle is higher in all models than at the end of the primary production. It demonstrates that the CO₂ huff-n-puff operation effectively supplements formation energy. This study further analyzes the degree of pressure sweep in different models. The confinement effect model exhibits the widest range of pressure sweep, followed by the molecular diffusion and no-mechanism models, which show similar characteristics. The pre-/post-Darcy model has a more limited pressure sweep range. The stress-sensitive model and the multi-mechanism model have the smallest pressure sweep ranges.

Fig. 20 shows the variations in BHP over time. Stress sensitivity and pre-/post-darcy flow increase BHP during the injection period. It can enhance production performance. Fig. 21(a) shows that stress sensitivity and pre-/post-Darcy flows led to 31.28% and 9.29% decrease in cumulative oil production (i.e., well oil production total,



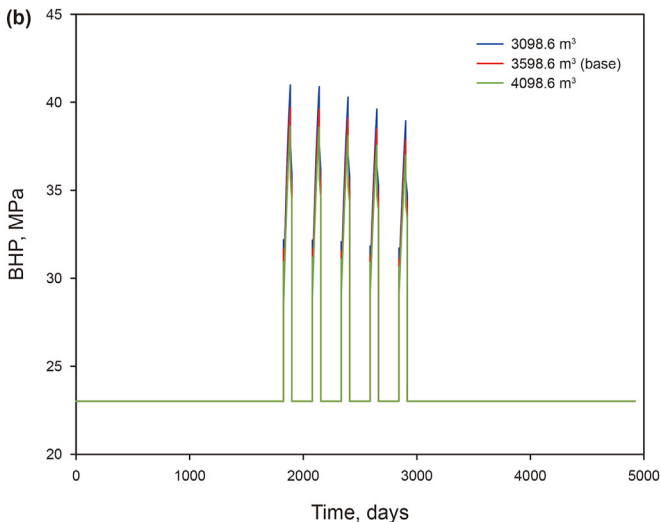


Fig. 25. The BHP change curves in the life-cycle process. (a) BHP change curve in fracturing and shut-in periods; (b) BHP change curve in the primary and huff-n-puff periods.

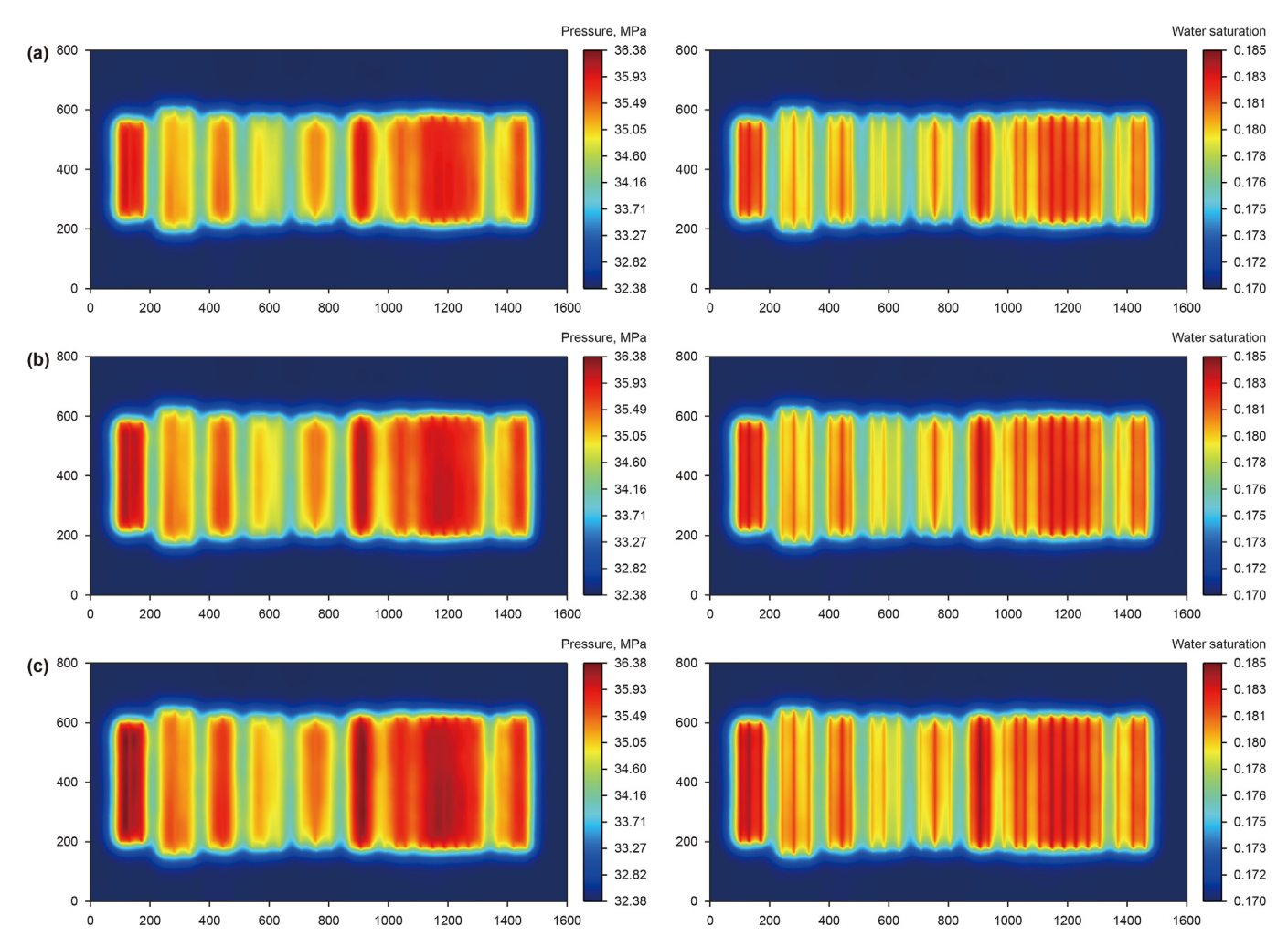


Fig. 26. The distribution of pressure (left) and water saturation (right) in the second layer at different fluid volumes at the end of the shut-in. (a) Case 1; (b) case 2; (c) case 3.

Table 11The effect of fracturing fluid volume on production, NPV, UF, and SF.

	WOPT, 10 ⁴ m ³	WGPT, 10 ⁶ m ³	NPV, 10 ⁶ \$	UF, m ³ /t	SF, t/t
3098.6 m ³ (case 1)	20.98	16.38	55.20	1.41	0.57
3098.6 m ³ -primary	11.91	0	34.78	_	_
3598.6 m ³ (case 2-base)	22.91	12.24	60.70	1.51	0.59
3598.6 m ³ -primary	13.33	0	39.17	_	_
4098.6 m ³ (case 3)	23.51	18.77	63.07	1.47	0.61
4098.6 m ³ -primary	14.73	0	43.46	-	_

WOPT) during the 5-year primary production process. However, during the CO₂ huff-n-puff process, the negative impact of these effects gradually diminished due to effective pressure supplementation. At the end of the simulation, both only reduces the production by 0.11% and 1.43%, respectively. Fig. 21(a) also indicates that incorporating the nano-confinement effect increases WOPT by 31.12% over 4922 days. The nano-confinement effect significantly enhances oil production. The impact of molecular diffusion on WOPT is minimal, resulting in only a 0.26% increase. The role of molecular diffusion may be overestimated (Sun et al., 2016). It is potentially due to the low diffusion coefficient of the liquid phase, which restricts the injected CO₂ to the stimulated reservoir volume (SRV) region, as shown in Fig. 22.

Fig. 21(b) illustrates the effect of different mechanisms on cumulative gas production (i.e., well gas production total, WGPT). The

results indicate that the nano-confinement effect reduced gas production by lowering the bubble point pressure. The stress sensitivity and pre-/post-Darcy flow reduced gas production by decreasing the gas phase flux. According to the data in Table 9, these three effects reduced WGPT by 55.59%, 52.20%, and 13.94%, respectively. When considering multi-mechanism coupling, there is a complex dynamic relationship between the mechanisms that inhibit or promote each other. Strong interactions between multiple mechanisms can result in complex production performance. Under the effect of multi-mechanisms, WOPT increased by 12.01%. However, the WGPT is the smallest, reduced by 81.02%. This reduction is likely due to the nano-confinement effect increasing the pressure drop in the SRV region, exacerbating stress sensitivity and the pre-/post-Darcy flow.

Fig. 23(a) illustrates the effects of different mechanisms on the

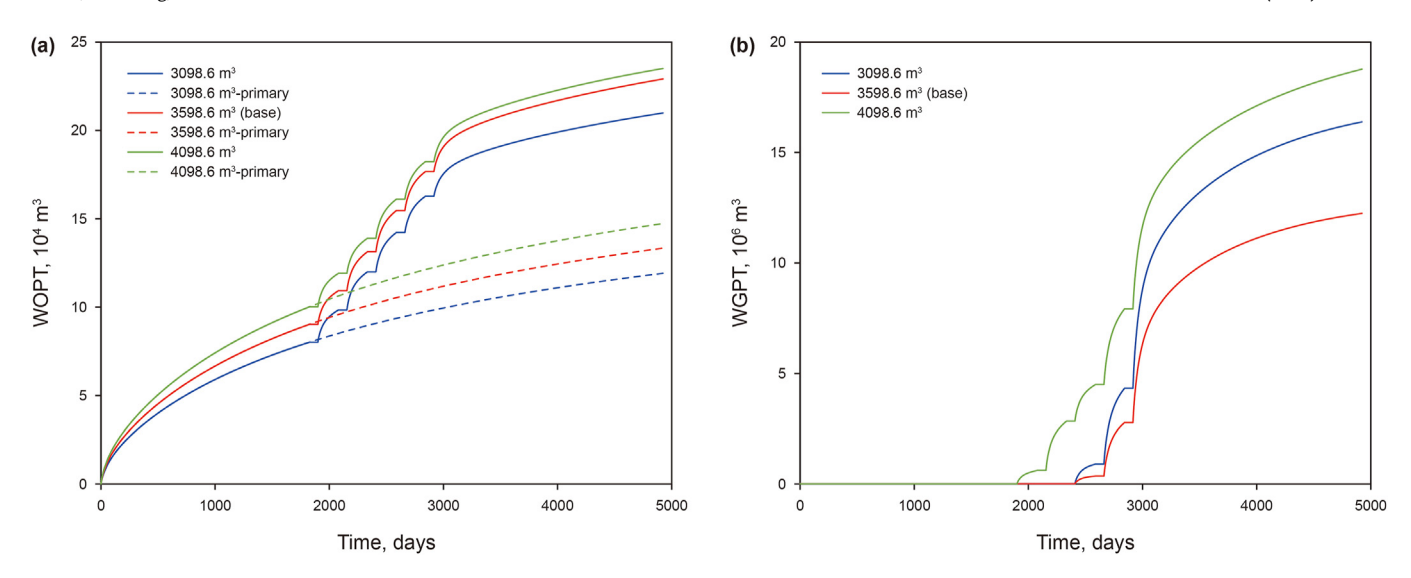


Fig. 27. The effect of fracturing fluid volume on WOPT (a) and WGPT (b).

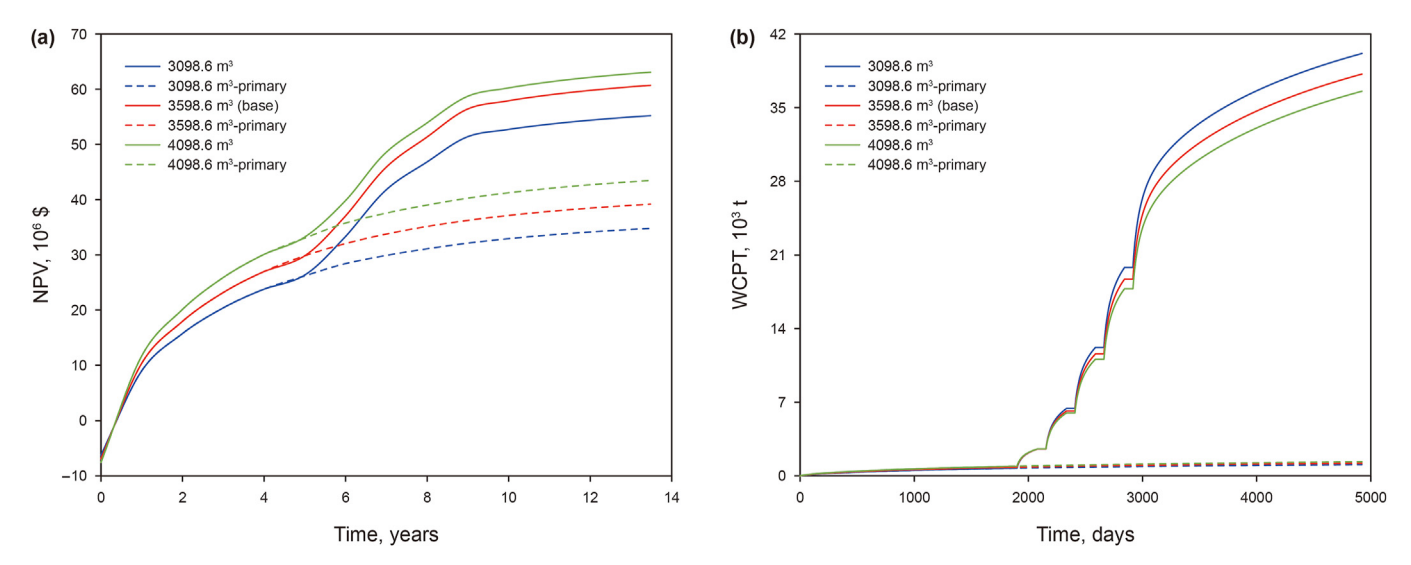


Fig. 28. The effect of fracturing fluid volume on NPV (a) and WCPT (b).

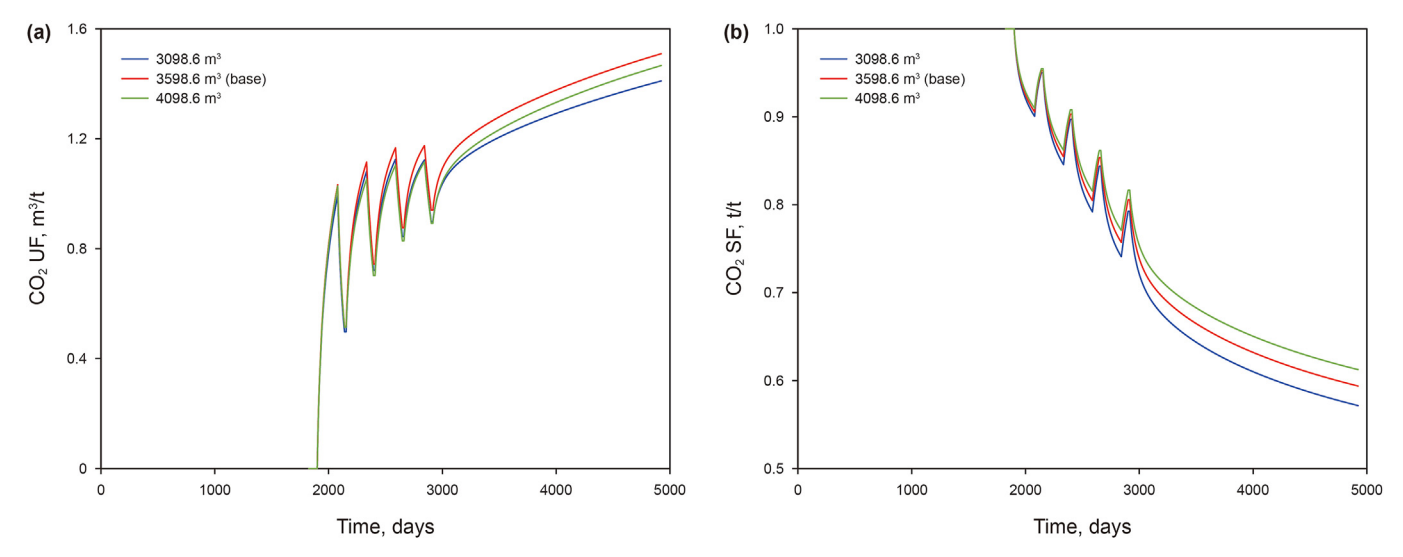


Fig. 29. The effect of fracturing fluid volume on CO_2 UF (a) and CO_2 SF (b).

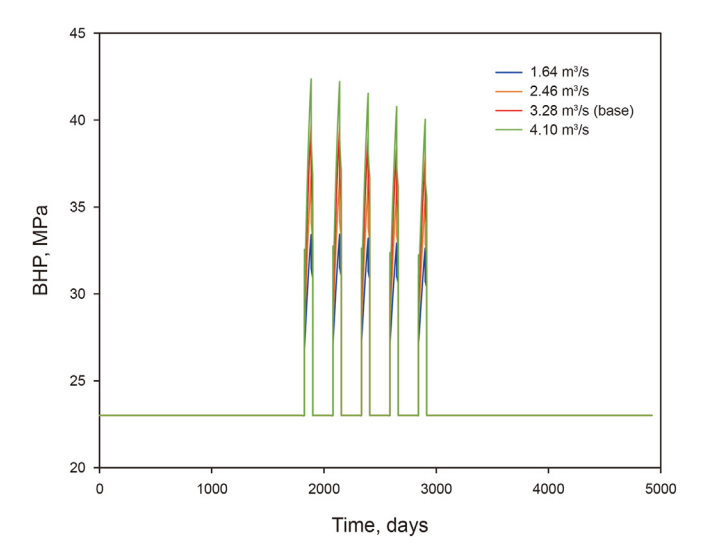


Fig. 30. The effect of CO₂ injection rate on BHP.

NPV. The results indicate that the nano-confinement effect significantly increased NPV by 28.63%. Conversely, stress sensitivity negatively impacted NPV, leading to a 10.78% decrease. The NPV of the multi-mechanism model during the primary depletion production period is similar to that of the stress-sensitive model. After the CO₂ huff-n-puff process, the NPV of the multi-mechanism model aligns more closely with the no-mechanism model. Fig. 23(b) shows the effect of different mechanisms on cumulative CO₂ production (well CO₂ production total, WCPT). The results reveal that the stress-sensitive and multi-mechanism models reduce WCPT by 5.34% and 10.77%, respectively. This reduction is

advantageous for CO2 storage.

Fig. 24 illustrates the changes in CO_2 UF and CO_2 SF over time. At the onset of CO_2 injection, the $P_{V,Oil}$, and P_{m,CO_2} are zero, leading to the lowest CO_2 UF and the highest CO_2 SF. As immiscible CO_2 -EOR progresses, the CO_2 UF increases, and the CO_2 SF decreases. The multi-mechanism model exhibits the highest CO_2 UF and CO_2 SF, with values of 1.45 and 0.61, respectively. In contrast, the no-mechanism model's CO_2 UF and CO_2 SF are the smallest, at 0.89 and 0.56, respectively. When considering multiple mechanisms, the CO_2 UF and CO_2 SF increase by 62.93% and 8.93%, respectively.

4. Results and analysis

This section discusses the impact of operating parameters, such as fracturing fluid volume, CO₂ injection rate, CO₂ injection time, and number of cycles, on production and storage performance. The analysis will consider the impact of fracturing and shut-in periods on the seepage field and production performance. This study set up one or more control groups for each sensitive factor to evaluate the effectiveness of CO₂ huff-n-puff technique. The control group is developed at a constant BHP of 23.01 MPa (i.e., without CO₂ huff-n-puff). The basic parameters and reservoir model are consistent with Section 3.2.

4.1. Fracturing fluid volume

Three fluid volume schemes are designed to study the effect of the fracturing period on the reservoir seepage field and CCUS-EOR. Table 10 shows each scheme's fracture height, length, displacement, dimensionless time, and fracturing fluid volume parameters. The average fluid volumes for the three groups are as follows: 3098.6 m³ (case 1), 3598.6 m³ (case 2, base case), and 4098.6 m³ (case 3). Additionally, three primary recovery control groups are set

5000

Table 12The effect of CO₂ injection rate on production, NPV, UF, and SF.

	WOPT, 10 ⁴ m ³	WGPT, 10 ⁶ m ³	NPV, 10 ⁶ \$	UF, m³/t	SF, t/t
1.64 m ³ /s (case 1)	17.54	9.78	49.18	1.41	0.57
2.46 m ³ /s (case 2)	20.52	8.65	55.23	1.67	0.64
3.28 m ³ /s (case 3-base)	22.91	12.24	60.70	1.51	0.59
4.10 m ³ /s (case 4)	24.03	26.46	63.28	1.30	0.55
Primary	13.33	0	39.17	-	_

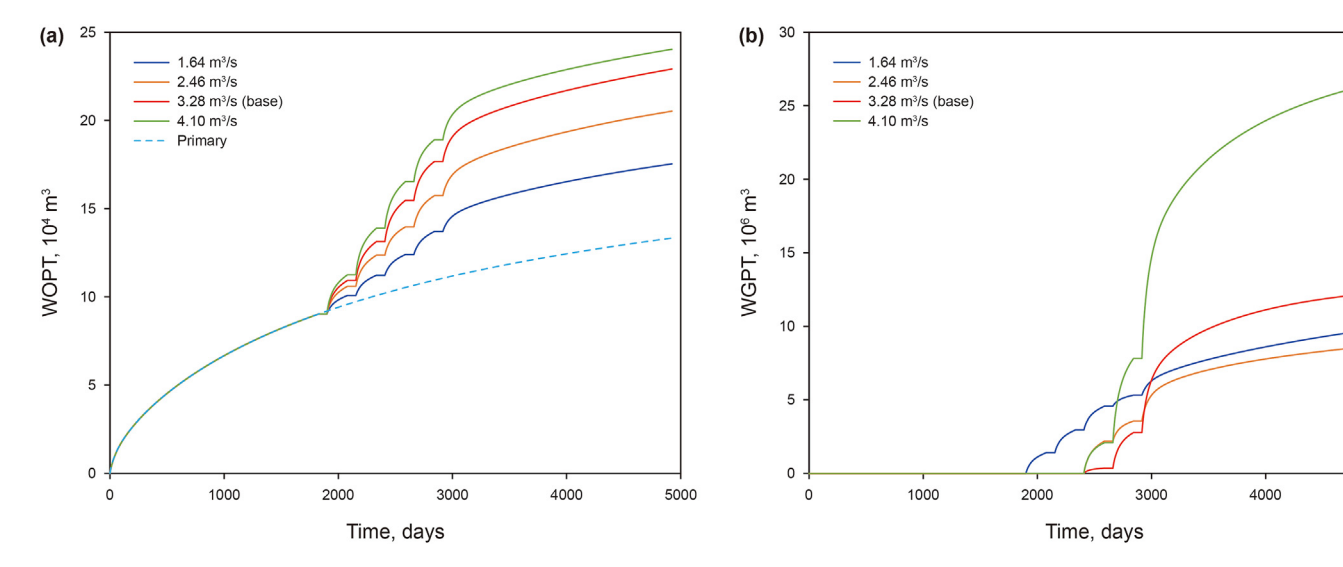


Fig. 31. The effect of CO_2 injection rate on WOPT (a) and WGPT (b).

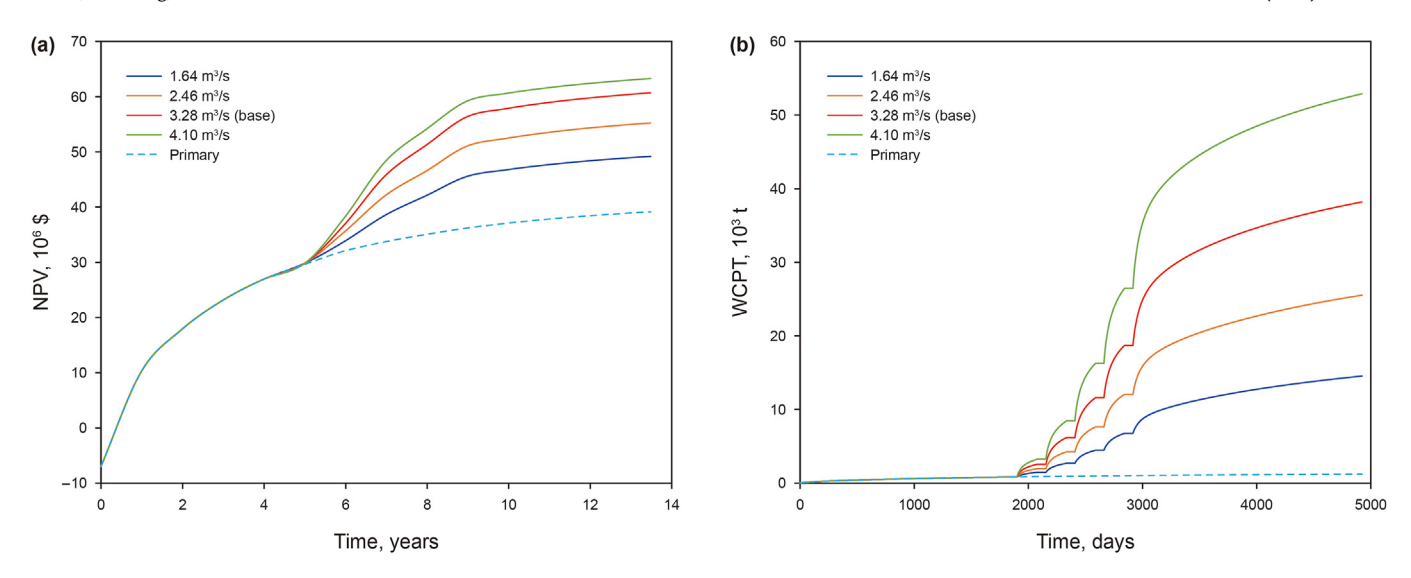


Fig. 32. The effect of CO₂ injection rate on NPV (a) and WCPT (b).

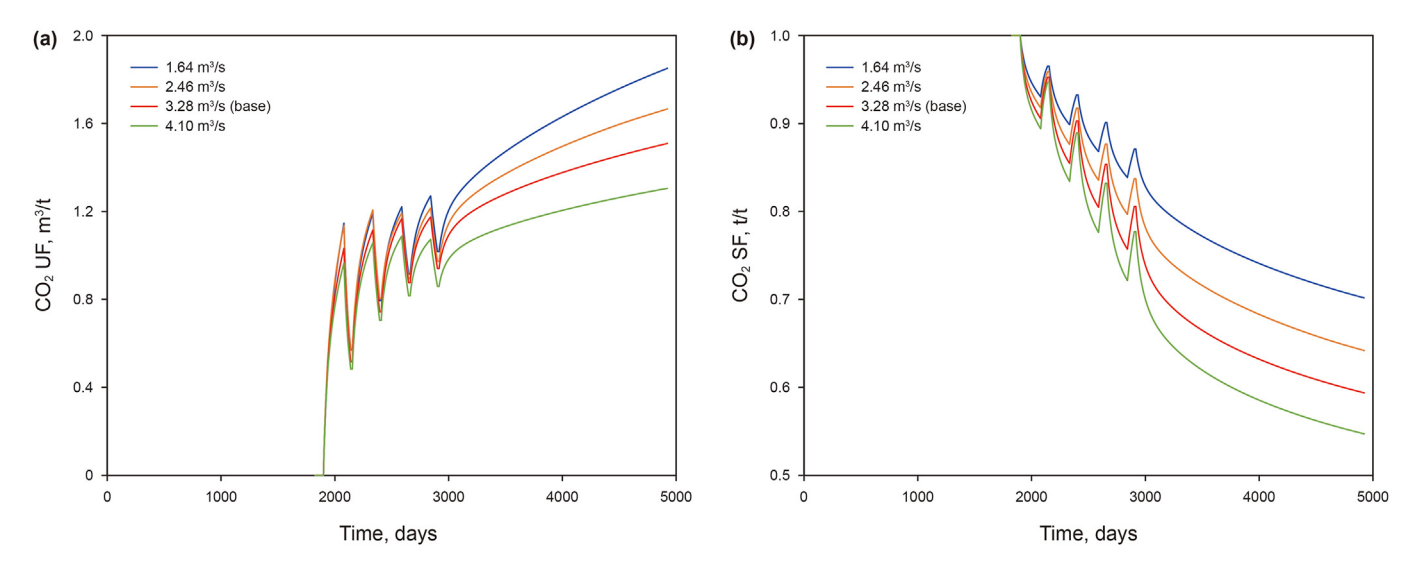


Fig. 33. The effect of CO_2 injection rate on CO_2 UF (a) and CO_2 SF (b).

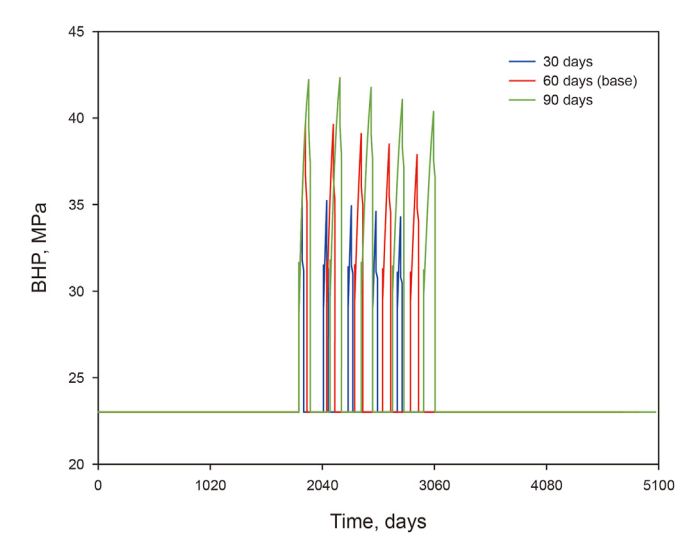


Fig. 34. The effect of CO₂ injection time on BHP.

for three cases. The dimensionless time range of the three fracturing schemes is between 0.001 and 0.028. Therefore, in this study, the leak-off effect can be ignored.

After the multi-stage fracturing operation, a 10-day shut-in process will be carried out, followed by primary depletion production. Fig. 25 reports the changes in BHP under three fluid volume schemes. Fig. 25(a) demonstrates that the BHP stabilizes after ten shut-in days. Fig. 25(b) indicates that a smaller fluid volume results in higher BHP under the same injection conditions.

Fig. 26 depicts the pressure and water saturation distribution for three different fluid volumes at the end of the shut-in period. Fig. 26 demonstrates that with the increase of fracturing fluid volume, the fracture length increases significantly, and the pressure and water saturation near SRV increase.

Compared to the multi-mechanism model discussed in Section 3.2, energy storage fracturing technology increases WOPT by 12.47% and the NPV by 15.07%. According to the data in Table 11, the WOPT for cases 1, 2, and 3 is 1.76, 1.72, and 1.69 times that of primary production, respectively. Similarly, the NPV for cases 1, 2, and 3 is 1.59, 1.55, and 1.45 times that of primary production,

Table 13The effect of CO₂ injection time on production, NPV, UF, and SF.

	WOPT, 10 ⁴ m ³	WGPT, 10 ⁶ m ³	NPV, 10 ⁶ \$	UF, m ³ /t	SF, t/t
30 days (case 1)	18.43	2.52	51.27	2.04	0.70
30 days-primary	13.20	0	38.99	_	_
60 days (case 2-base)	22.91	12.24	60.70	1.51	0.59
60 days-primary	13.33	0	39.17	_	_
90 days (case 3)	24.65	42.92	63.07	1.13	0.51
90 days-primary	13.46	0	43.46	_	_

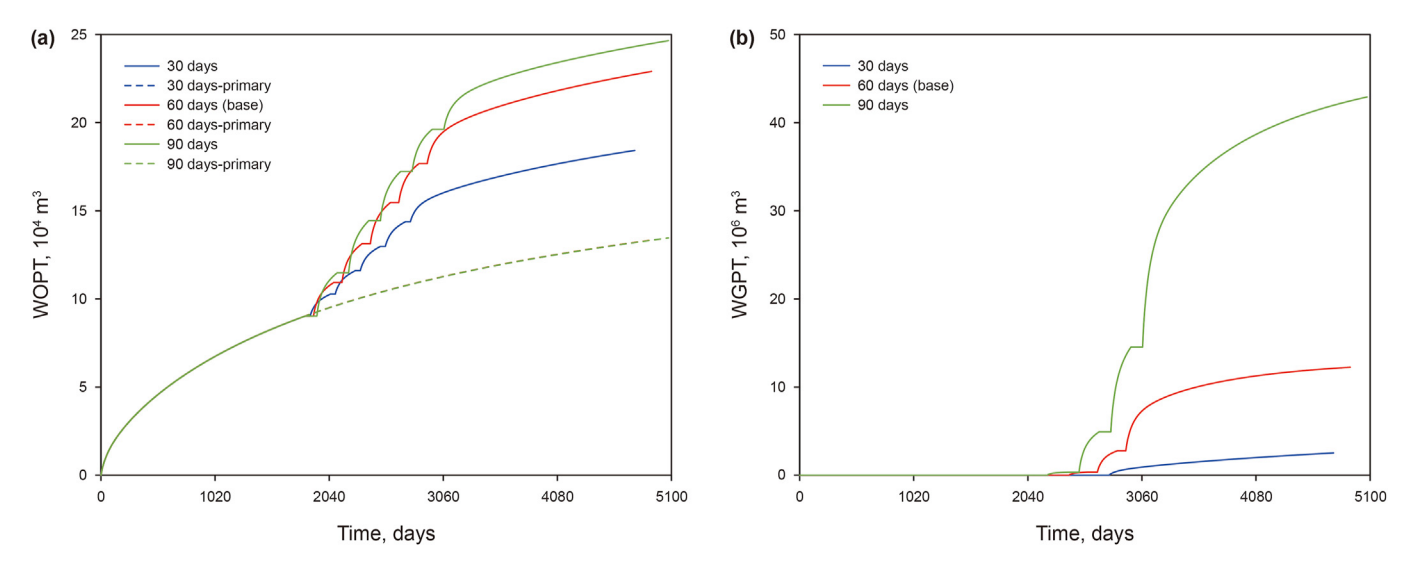


Fig. 35. The effect of CO_2 injection time on WOPT (a) and WGPT (b).

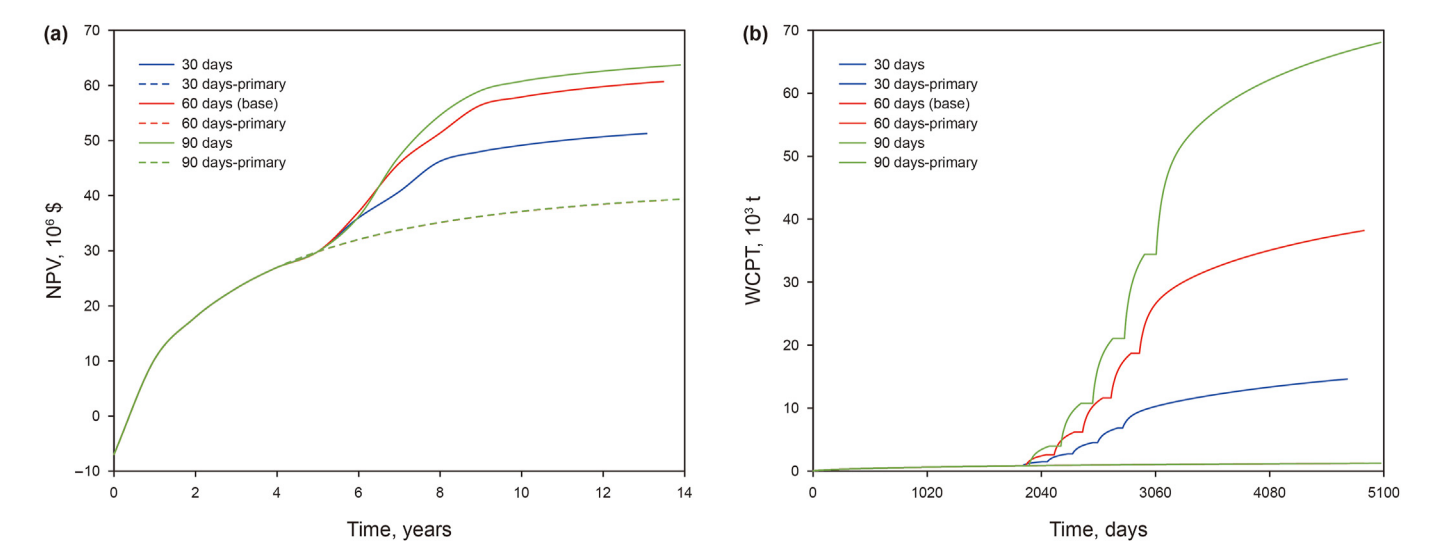
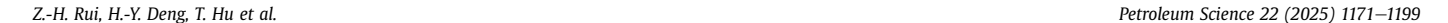


Fig. 36. The effect of CO₂ injection time on NPV (a) and WCPT (b).

respectively. Figs. 27(a) and 28(a) indicate that within the parameter range of this study, the fracturing fluid volume is positively correlated with WOPT and NPV. However, when the average fluid volume reaches 3598.6 m³, the increment of WOPT and NPV decreases significantly with the further increase of fracturing fluid volume. Fig. 27(b) illustrates the effect of fracturing fluid volume on WGPT. Case 3 exhibits the longest fracture length, the earliest gas breakthrough, and the highest WGPT. Despite having the shortest fracture length, case 1 exhibits higher BHP than case 2 during the

injection period. As a result, the WGPT of case 1 exceeds that of case 2. Fig. 28(b) demonstrates a negative correlation between the fracturing fluid volume and WCPT. It indicates that increased fracturing fluid volume can enhance CO_2 storage (i.e., higher CO_2 SF value). This correlation is further illustrated in Fig. 29(b). During the huff-n-puff period, the WOPT for case 2 is 13.88×10^4 m³, slightly higher than that for case 3 (13.48×10^4 m³). Case 2 achieves higher oil production performance (i.e., higher CO_2 UF value) at the same CO_2 injection volume, as shown in Fig. 29(a).



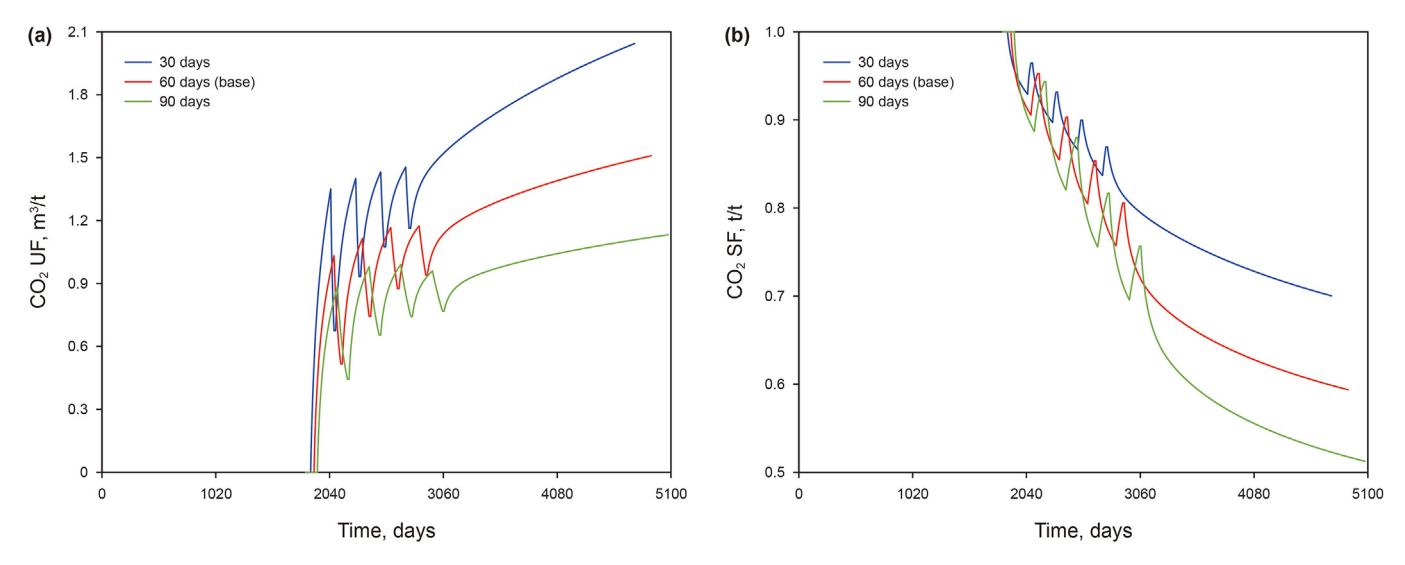


Fig. 37. The effect of CO_2 injection time on CO_2 UF (a) and CO_2 SF (b).

Table 14The effect of the number of cycles on production, NPV, UF, and SF.

	WOPT, 10 ⁴ m ³	WGPT, 10 ⁶ m ³	NPV, 10 ⁶ \$	UF, m³/t	SF, t/t
3 cycles (case 1)	20.32	0.41	55.18	2.05	0.64
5 cycles (case 2-base)	23.44	12.52	61.33	1.57	0.58
7 cycles (case 3)	25.23	36.46	64.48	1.26	0.52
Primary	13.75	0	39.69	_	_

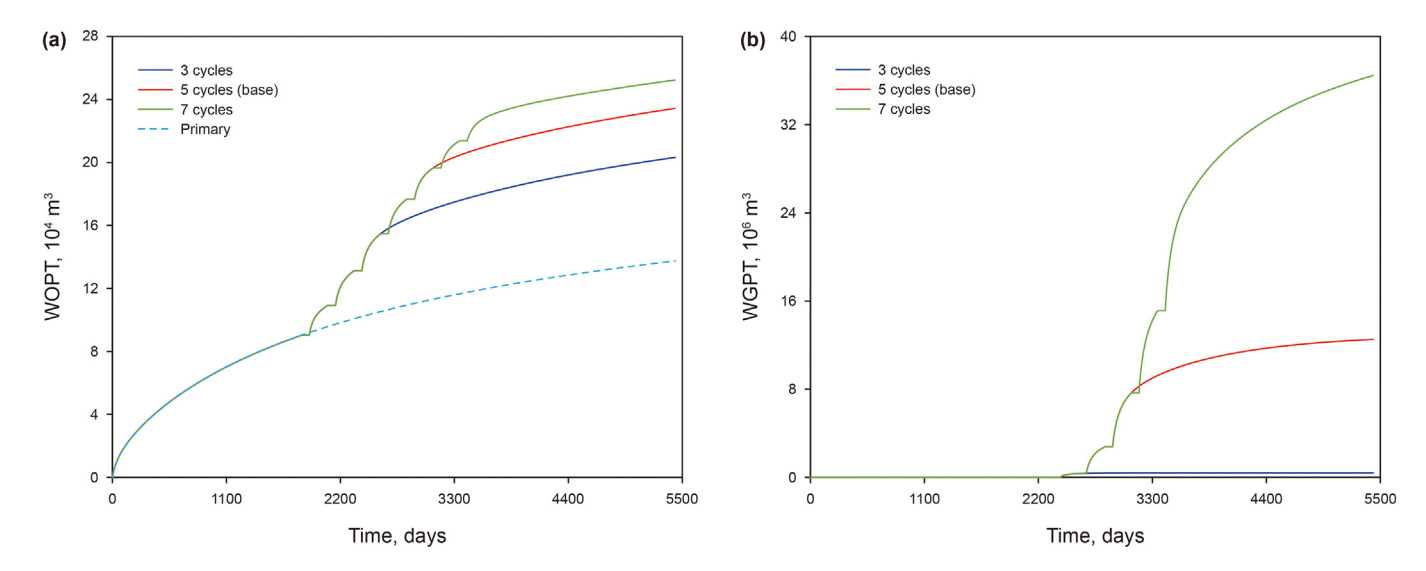


Fig. 38. The effect of the number of cycles on WOPT (a) and WGPT (b).

Increasing the fracturing fluid volume has positively affected the development of shale oil reservoirs by enhancing energy storage fracturing and increasing the SRV. However, unfavorable aspects, such as formation damage from excessive fracturing fluid injection, cannot be ignored. Furthermore, the shorter the fracture, the higher the BHP, which benefits the production performance.

4.2. CO₂ injection rate

The CO_2 injection rate is an important operating parameter in the CO_2 huff-n-puff process. The injection rate significantly affects

CO₂-EOR and storage capacity. Four different injection rate schemes are designed, namely $1.64~\text{m}^3/\text{s}$ (case 1), $2.46~\text{m}^3/\text{s}$ (case 2), $3.28~\text{m}^3/\text{s}$ (case 3, base), and $4.10~\text{m}^3/\text{s}$ (case 4), to analyze the effect of injection rate on different indices. The remaining design parameters are consistent with the basic parameters. Moreover, this work sets a primary recovery control group for four cases.

Fig. 30 reports the change in BHP at different injection rates. The BHP rises as the injection rate increases. When the injection rate is $1.64~{\rm m}^3/{\rm s}$, the maximum BHP is close to the initial formation pressure. However, if the injection rate exceeds $4.10~{\rm m}^3/{\rm s}$, the BHP may be higher than the formation fracture pressure or ground

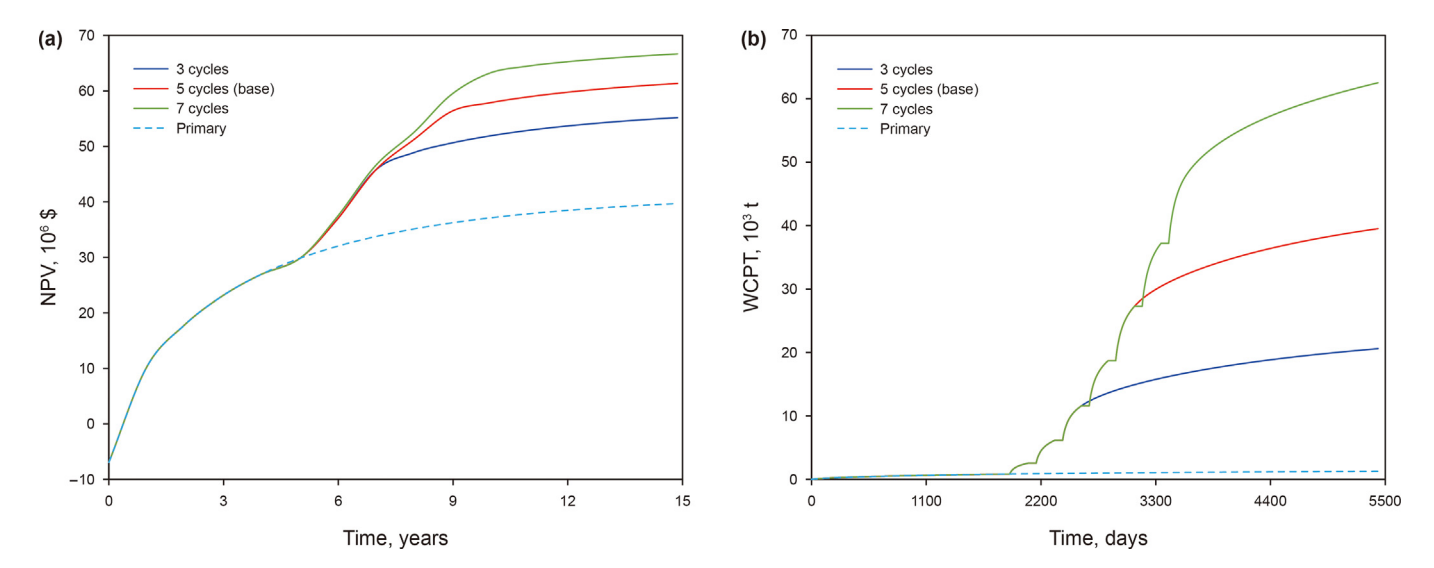


Fig. 39. The effect of the number of cycles on NPV (a) and WCPT (b).

equipment load. It potentially causes equipment damage or gas channeling.

According to the data in Table 12, the WOPT for cases 1 to 4 is 1.32, 1.54, 1.72, and 1.80 times that of primary production, respectively. Similarly, the NPV is 1.26, 1.41, 1.54, and 1.62 times that of the primary output. There is a positive correlation between the CO_2 injection rate and both WOPT and NPV, as shown in Figs. 31 and 32. However, when the injection rate exceeds 3.28 m³/s, the incremental production increases, and NPV significantly diminishes. For an injection rate of 1.64 m³/s (case 1), the repressurization effect is not apparent, and the gas breakthrough time is the earliest. The WOPT of case 1 (1.64 m³/s) exceeds that of case 2 (2.46 m³/s), as illustrated in Fig. 31(b).

Fig. 33 shows a negative correlation between the CO_2 injection rate and the CO_2 UF and CO_2 SF. In other words, as the injection rate increases, the utilization and storage rates of CO_2 decrease. Based on these evaluation indices, the injection rate of 3.28 m³/s is the optimal gas injection rate.

4.3. CO₂ injection time

The CO₂ injection time is an important design parameter that affects gas cycle performance and development economy. This section sets three sets of injection times: 30 days (case 1), 60 days (case 2, base), and 90 days (case 3). Fig. 34 illustrates the changes in BHP under different injection times. Similarly, this paper sets primary recovery control groups corresponding to different injection times. The results show that, similar to the injection rate, the longer the injection time, the higher the BHP.

Table 13 shows that the WOPT for cases 1 to 3 is 1.40, 1.72, and 1.83 times that of the corresponding primary production, respectively, while the NPV is 1.31, 1.55, and 1.45 times that of the corresponding primary production. Figs. 35 and 36 further illustrate the positive correlation between WOPT, WGPT, NPV, WCPT, and CO₂ injection time. Specifically, when the injection time increases from 30 to 60 days, there is a significant increase in WOPT and NPV. However, when the injection time increases from 60 to 90 days, the rise in WOPT and NPV is relatively tiny. Fig. 37 reports that longer injection times decrease CO₂ flooding and storage capacity. For the

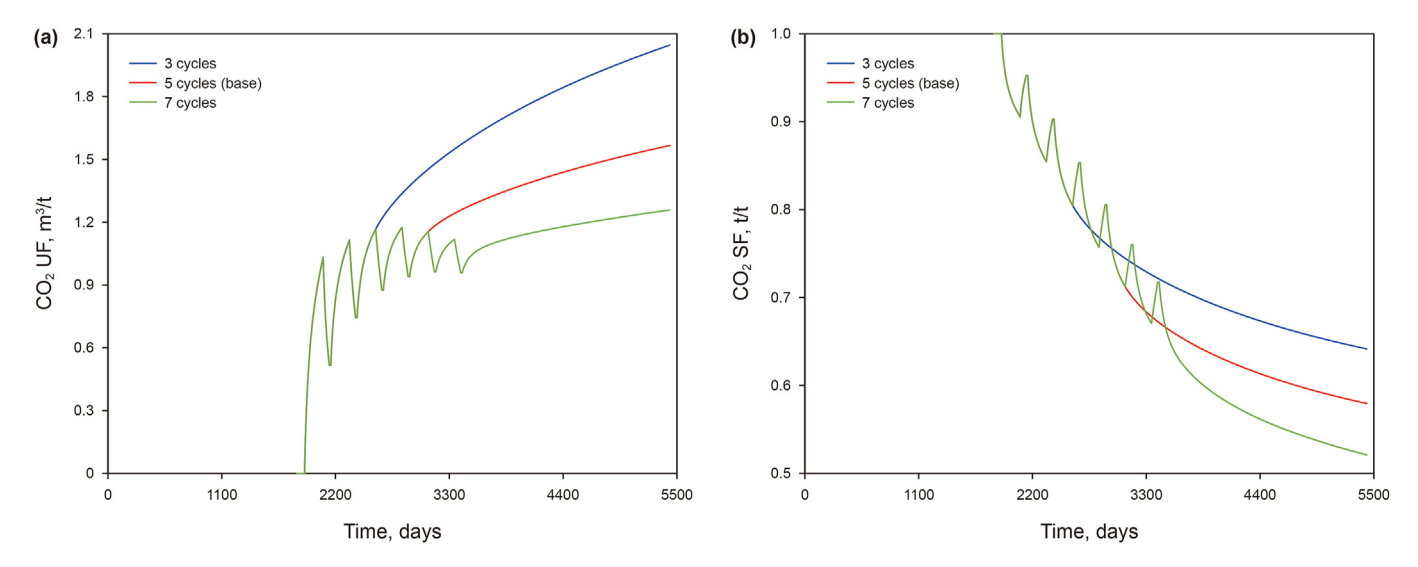


Fig. 40. The effect of the number of cycles on CO_2 UF (a) and CO_2 SF (b).

injection rate of 3.28 m³/s, an injection time of 60 days is optimal.

4.4. Number of cycles

The number of cycles is an essential operating parameter in the CO_2 huff-n-puff process. In this study, the number of cycles is set to 3 (case 1), 5 (case 2, base), and 7 (case 3) to examine its effects on production performance, NPV, and CCUS-EOR. To ensure consistency in simulation time for different schemes, the continuing production time is extended by 1016 and 508 days after the end of the 3-cycle and 5-cycle huff-n-puff processes, respectively. Moreover, this work sets a primary recovery control group for the number of cycles.

According to the data in Table 14, the WOPT for cases 1 to 3 is 1.48, 1.70, and 1.83 times that of primary production, respectively. The NPV is 1.39, 1.55, and 1.62 times that of the primary output. Figs. 38 and 39 demonstrate the positive correlation between WOPT, WGPT, NPV, WCPT, and the number of cycles. Specifically, WGPT increased significantly with the number of cycles. Fig. 40 indicates that the CO_2 UF and CO_2 SF decrease as cycles increase. Increasing the number of cycles can enhance WOPT and WGPT but can reduce CO_2 storage capacity. Moreover, within the scope of this study, increasing the number of cycles did not significantly diminish the incremental production and NPV. Therefore, without special consideration of oil displacement and storage capacity, a moderate increase in the number of cycles is an effective approach for achieving CO_2 -EOR.

4.5. Comparison of sensitivity analysis

Based on the above sensitivity analysis, this section further analyzes the main mechanisms and operating factors affecting the oil recovery factor (RF). Fig. 41 summarizes the effects of singlemechanism and multi-mechanism models on the incremental RF at different time points. The results are obtained and compared with those of the no-mechanism model. During the primary production process, the RF of the multi-mechanism model is mainly negatively affected by stress sensitivity. However, during the CO₂ huff-n-puff process, the negative impact of stress sensitivity and the pre-/post-Darcy flow diminishes. At this point, the RF of the multi-mechanism model is mainly driven by the positive effect of the nano-confinement effect. The impact of molecular diffusion on RF is relatively minor. The mechanism analysis results align with those reported by Wang et al. (2024). Therefore, they did not observe the difference in mechanism contribution at different periods.

Fig. 42 summarizes the effect of each operating parameter on

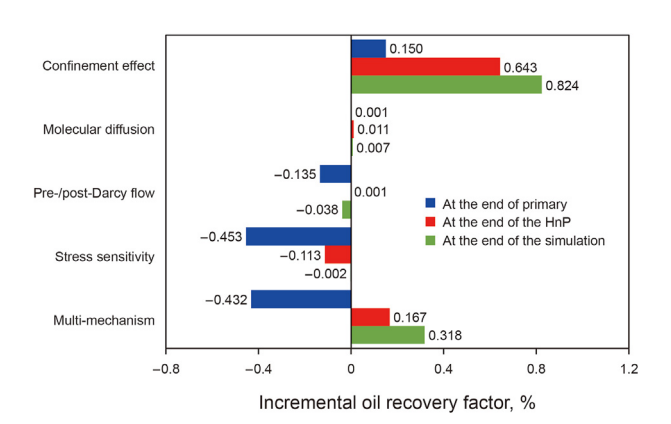


Fig. 41. The order of mechanism factors affecting incremental oil recovery factor.

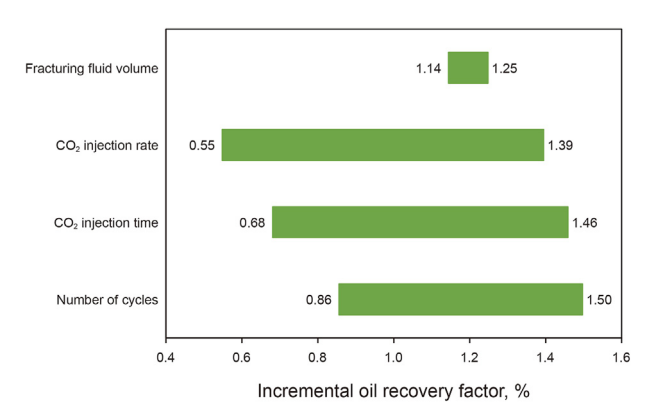


Fig. 42. The order of operating factors affecting incremental oil recovery factor.

the incremental RF compared to the primary production parameters. In this study, the range of incremental RF is 0.55%-1.50%. The analysis results indicate that the RF increases with the fracturing fluid volume, CO_2 injection rate, CO_2 injection time, and number of cycles. Among these, the CO_2 injection rate has the most significant impact on the RF, followed by the CO_2 injection time and the number of cycles, and the fracturing fluid volume has the least impact.

4.6. Limitations

This study proposes a multi-mechanism integrated simulation model for the full-cycle fracturing and development of shale oil reservoirs, several limitations should be acknowledged.

- (1) The dynamic propagation of fractures is simplified as the injection process of fixed bi-wing fractures. This simplification arises from the inherent difficulty of fully coupling fluid flow with fracture propagation. Moreover, this study ignores the impact of partial fracture closure on production performance during the shut-in period.
- (2) The phenomenon of non-Darcy flow in shale oil reservoirs remains an emerging research field. The applicability of multiple mechanisms (nano-confinement effect, molecular diffusion, pre-/post-Darcy flow, and stress sensitivity) to specific reservoirs needs further experimental validation. Moreover, these mechanisms may not adequately capture the intricate fluid behavior observed in shale oil reservoirs.
- (3) The simulation results have not been validated with field data. Future research work will integrate on-site data to enhance the credibility of the results.

5. Conclusions

This study proposes a life-cycle multi-component numerical simulation model designed to evaluate the performance of CCUS-EOR. This model can realize the integrated simulation of fracturing, shut-in, depletion production, and CO₂ huff-n-puff processes. The integrated simulation approach ensures the continuity of the seepage field, thereby providing a more realistic description of the fracturing and development process. Furthermore, the PKN-EDFM method is used to characterize and simulate multi-stage fractures. During the subsequent development period, the model incorporates essential flow mechanisms of shale oil reservoirs, such as nano-confinement effect, molecular diffusion, pre-/post-Darcy flow, and stress sensitivity. This multi-process and multi-mechanism simulation framework can more accurately evaluate

production and storage performance. This study provides both a theoretical foundation and practical insights for the implementation of energy storage fracturing and CCUS-EOR in shale oil reservoirs. The main conclusions are as follows.

- A multi-dimensional evaluation system, including WOPT, RF, NPV, CO₂ UF, and CO₂ SF, is established to evaluate the performance of CCUS-EOR.
- (2) Compared to the no-mechanism model, stress sensitivity and pre-/post-Darcy flow reduce WOPT by 31.28% and 9.29% during the primary production process. However, by the end of the simulation, these two effects only reduce WOPT by 0.11% and 1.43%. The results indicate that the CO₂ huff-n-puff mitigates these adverse effects on production performance. Furthermore, when considering only the confinement effect, WOPT increases by 31.12%, significantly enhancing well productivity. For the shale reservoir model used in this study, the impact of molecular diffusion on oil production is relatively small. When coupling multiple mechanisms, WOPT increases by 12.01%. Additionally, the multi-mechanism model has the highest CO₂ UF and CO₂ SF, which increases by 62.93% and 8.93%, respectively.
- (3) The effects of each mechanism on the RF are significantly different in different periods. During the primary production period, the RF of the multi-mechanism model is mainly negatively affected by stress sensitivity. However, during the CO₂ huff-n-puff period, the RF in the multi-mechanism model is mainly positively impacted by the nanoconfinement effect.
- (4) The multi-stage fracturing technology and post-fracturing shut-in strategy significantly affect the pressure and saturation distribution before primary depletion production. The energy storage fracturing technology can increase WOPT by 12.47% and NPV by 15.07%. A well-designed energy storage fracturing strategy can increase production and bring considerable economic benefits.
- (5) According to all the evaluation indexes, for the reservoir in this paper, the optimal gas injection rate is 3.28 m³/s, and the optimal gas injection time is 60 days. Moderately increasing the number of cycles is an effective approach for CO₂-EOR.
- (6) The sensitivity analysis results indicate that the most important parameter affecting the RF is the CO₂ injection rate, followed by CO₂ injection time and the number of cycles within the scope of this study. The least is the fracturing fluid volume. These results provide clear guidance for parameter optimization in CCUS-EOR and help decision-makers develop more effective gas injection strategies.

CRediT authorship contribution statement

Zhen-Hua Rui: Supervision, Resources, Funding acquisition, Conceptualization. **Hai-Yang Deng:** Writing — review & editing, Writing — original draft, Validation, Supervision, Software, Methodology, Conceptualization. **Ting Hu:** Writing — original draft, Project administration, Methodology, Funding acquisition, Data curation. **Guang-Long Sheng:** Writing — review & editing, Resources, Methodology, Investigation, Data curation. **Malcolm Wilson:** Supervision, Software, Resources, Project administration. **Birol Dindoruk:** Supervision, Investigation, Formal analysis, Data curation, Conceptualization. **Shirish Patil:** Validation, Supervision, Resources, Investigation, Formal analysis, Data curation.

Declaration of competing interest

The authors declare that they have no known competing financial interests or personal relationships that could have appeared to influence the work reported in this paper.

Acknowledgments

This study is supported by the National Natural Science Foundation of China (No. 52341401), the National Key Research and Development Program of China under grant (No. 2022YFE0206700), the National Natural Science Foundation of China (No. 42302272), the State-funded Postdoctoral Fellowship Program (No. GZB20230862), the Science Foundation of China University of Petroleum, Beijing (No. 2462023XKBH006), the Science Foundation of China University of Petroleum, Beijing (No. 2462021YJRC012) and the Open Project Program of Key Laboratory of Groundwater Resources and Environment (Jilin University), Ministry of Education (No. 202306ZDKF05). The authors thank Dr. Branko Bijeljic for the fruitful correspondence by answering the question we had regarding fluid diffusion in shale reservoir.

References

- Agada, S., Geiger, S., Doster, F., 2016. Wettability, hysteresis and fracture—matrix interaction during CO₂ EOR and storage in fractured carbonate reservoirs. Int. J. Greenh. Gas Control 46, 57–75. https://doi.org/10.1016/j.ijggc.2015.12.035.
- Alharthy, N.S., Nguyen, T.N., Teklu, T.W., et al., 2013. Multiphase compositional modeling in small-scale pores of unconventional shale reservoirs. In: SPE Annual Technical Conference and Exhibition. https://doi.org/10.2118/166306-MS
- Alramahi, B., Sundberg, M., 2012. Proppant embedment and conductivity of hydraulic fractures in shales. In: ARMA US Rock Mechanics/Geomechanics Symposium.
- Azin, R., Izadpanahi, A., 2022. Fundamentals and Practical Aspects of Gas Injection. Springer.
- Chen, D., Ye, Z.H., Pan, Z.J., et al., 2017. A permeability model for the hydraulic fracture filled with proppant packs under combined effect of compaction and embedment. J. Pet. Sci. Eng. 149, 428–435. https://doi.org/10.1016/ j.petrol.2016.10.045.
- Cheng, H., Wang, F., Guan, X., et al., 2023. A mathematical model for pre-Darcy flow in low permeability porous media with stress sensitivity and the boundary-layer effect. Eng. Geol. 324, 107257. https://doi.org/10.1016/j.enggeo.2023.107257.
- Danesh, A., Dandekar, A., Todd, A., et al., 1991. A modified scaling law and parachor method approach for improved prediction of interfacial tension of gascondensate systems. In: SPE Annual Technical Conference and Exhibition. https://doi.org/10.2118/22710-MS.
- Demidov, D., 2019. AMGCL: an efficient, flexible, and extensible algebraic multigrid implementation. Lobachevskii J. Math. 40 (5), 535–546. https://doi.org/10.1134/s1995080219050056.
- Dontsov, E.V., Peirce, A.P., 2017. A multiscale Implicit Level Set Algorithm (ILSA) to model hydraulic fracture propagation incorporating combined viscous, toughness, and leak-off asymptotics. Comput. Methods Appl. Mech. Eng. 313, 53–84. https://doi.org/10.1016/j.cma.2016.09.017.
- Fakcharoenphol, P., Torcuk, M., Kazemi, H., et al., 2016. Effect of shut-in time on gas flow rate in hydraulic fractured shale reservoirs. J. Nat. Gas Sci. Eng. 32, 109–121. https://doi.org/10.1016/j.jngse.2016.03.068.
- Fuller, E.N., Schettler, P.D., Giddings, J.C., 2002. New method for prediction of binary gas-phase diffusion coefficients. Ind. Eng. Chem. 58 (5), 18–27. https://doi.org/10.1021/ie50677a007.
- Geertsma, J., De Klerk, F., 1969. A rapid method of predicting width and extent of hydraulically induced fractures. J. Petrol. Technol. 21 (12), 1571–1581. https://doi.org/10.2118/2458-PA.
- Hu, T., Wang, Y., Xu, T., et al., 2023. A novel technique for quantifying the fate of CO₂ injected in oil reservoir for geological utilization and storage. Energy Rep. 9, 5350–5361. https://doi.org/10.1016/j.egyr.2023.04.364.
- Huang, J., Hao, Y., Settgast, R.R., et al., 2022. Validation and application of a three-dimensional model for simulating proppant transport and fracture conductivity. Rock Mech. Rock Eng. 56 (10), 7091–7113. https://doi.org/10.1007/s00603-022-03092-3
- Jahangiri, H.R., Zhang, D.X., 2012. Ensemble based co-optimization of carbon dioxide sequestration and enhanced oil recovery. Int. J. Greenh. Gas Control 8, 22–33. https://doi.org/10.1016/j.ijggc.2012.01.013.
- Javadpour, F., 2009. Nanopores and apparent permeability of gas flow in mudrocks (shales and siltstone). J. Can. Pet. Technol. 48 (8), 16–21. https://doi.org/10.2118/09-08-16-DA.

- Jia, Z.H., Cheng, L.S., Feng, H.R., et al., 2023. Full composition numerical simulation of CO₂ utilization process in shale reservoir using projection-based embedded discrete fracture model (pEDFM) considering nano-confinement effect. Gas Sci. Eng. 111, 204932. https://doi.org/10.1016/j.jgsce.2023.204932.
- Lie, K.A., 2019. An Introduction to Reservoir Simulation Using MATLAB/GNU Octave: User Guide for the MATLAB Reservoir Simulation Toolbox (MRST). Cambridge University Press.
- Lie, K.A., Møyner, O., 2021. Advanced Modelling with the MATLAB Reservoir Simulation Toolbox. Cambridge University Press.
- Liu, Y.L., Hu, T., Rui, Z.H., et al., 2023. An integrated framework for geothermal energy storage with CO₂ sequestration and utilization. Engineering 30, 121–130. https://doi.org/10.1016/j.eng.2022.12.0102095-8099.
- Lohrenz, J., Bray, B.G., Clark, C.R., 1964. Calculating viscosities of reservoir fluids from their compositions. J. Petrol. Technol. 16 (10), 1171-1176. https://doi.org/ 10.2118/915-PA.
- Mallison, B.T., Gerritsen, M.G., Jessen, K., et al., 2005, High-order upwind schemes for two-phase, multicomponent flow. SPE J. 10 (3), 297-311. https://doi.org/ 10.2118/79691-OA.
- Martin, I.I., 1979. Cubic equations of state-which? Ind. Eng. Chem. Fundam. 18 (2), 81-97. https://doi.org/10.1021/i160070a001.
- Moinfar, A., Varavei, A., Sepehrnoori, K., et al., 2014. Development of an efficient embedded discrete fracture model for 3D compositional reservoir simulation in fractured reservoirs. SPE J. 19 (2), 289–303. https://doi.org/10.2118/154246-PA.
- Niu, Y., Wang, Y., Li, J., et al., 2022. Effects of forward and reverse shear displacements on geometric and hydraulic characteristics of single rough fracture by the finite volume method. Lithosphere 2021 (Special 3), 7799052. https:// doi.org/10.2113/2022/7799052.
- Nordgren, R.P., 1972. Propagation of a vertical hydraulic fracture. Soc. Petrol. Eng. J.
- 12 (4), 306–314. https://doi.org/10.2118/3009-PA.
 Olorode, O.M., Akkutlu, I.Y., Efendiev, Y., 2017. Compositional reservoir-flow simulation for organic-rich gas shale. SPE J. 22 (6), 1963-1983. https://doi.org/ 10.2118/182667-PA
- Olorode, O., Wang, B., Rashid, H.U., 2020. Three-dimensional projection-based embedded discrete-fracture model for compositional simulation of fractured reservoirs. SPE J. 25 (4), 2143-2161. https://doi.org/10.2118/201243-PA.
- Olorode, O., Amer, H., Rashid, H., 2021. The role of diffusion in primary and enhanced oil recovery from fractured unconventional reservoirs. In: Asia Pacific Unconventional Resources Technology Conference. https://doi.org/10.15530/apurtec-2021-208387.
- Poling, B.E., Prausnitz, J.M., O'connell, J.P., 2001. The Properties of Gases and Liquids. Mcgraw-hill, New York.
- Prada, A., Civan, F., 1999. Modification of Darcy's law for the threshold pressugradient. J. Pet. Sci. Eng. 22 (4), 237-240. https://doi.org/10.1016/s0920-4105(98)00083-7
- Ratnakar, R.R., Dindoruk, B., 2022. The role of diffusivity in oil and gas industries: fundamentals, measurement, and correlative techniques. Processes 10 (6), 1194. https://doi.org/10.3390/pr10061194.
- Rezaveisi, M., Javadpour, F., Sepehrnoori, K., 2014. Modeling chromatographic separation of produced gas in shale wells. Int. J. Coal Geol. 121, 110-122. https:// doi.org/10.1016/j.coal.2013.11.005
- Shao, J., Zhang, Q., Sun, W., et al., 2020. Numerical simulation on non-Darcy flow in a single rock fracture domain inverted by digital images. Geofluids 2020 (1), 1-13. https://doi.org/10.1155/2020/8814327
- Shen, L., Chen, Z., 2007. Critical review of the impact of tortuosity on diffusion. Chem. Eng. Sci. 62 (14), 3748-3755. https://doi.org/10.1016/j.ces.2007.03.041.
- Sheng, G.L., Deng, H.Y., Zhao, H., et al., 2023a. Life cycle integrated flow simulation for hydraulic fracturing horizontal wells in shale gas reservoirs. Phys. Fluids 35 (10), 103318. https://doi.org/10.1063/5.0170045.
- Sheng, G.L., Zhao, H., Huang, L.Y., et al., 2023b. A real-time inversion approach for fluid-flow fractures in unconventional stimulated reservoirs. SPE J. 29 (2), 1178-1194. https://doi.org/10.2118/218001-PA.
- Sheng, G.L., Zhao, H., Huang, L.Y., et al., 2024. A real-time inversion approach for fluid- flow fractures in unconventional stimulated reservoirs. SPE J. 29 (2), 1178-1194. https://doi.org/10.2118/218001-PA.
- Shi, J.Q., Durucan, S., 2016. Near-exponential relationship between effective stress and permeability of porous rocks revealed in Gangi's phenomenological models and application to gas shales. Int. J. Coal Geol. 154, 111-122. https://doi.org/ 10.1016/i.coal.2015.12.014.
- Singh, H., Cai, J.C., 2018. Screening improved recovery methods in tight-oil formations by injecting and producing through fractures. Int. J. Heat Mass Tran. 116, 977-993. https://doi.org/10.1016/j.ijheatmasstransfer.2017.09.071.
- Song, Z.J., Song, Y.L., Guo, J., et al., 2021. Effect of nanopore confinement on fluid phase behavior and production performance in shale oil reservoir. Ind. Eng. Chem. Res. 60 (3), 1463–1472. https://doi.org/10.1021/acs.iecr.0c05814.
- Sun, H., Chawathé, A., Hoteit, H., et al., 2015. Understanding shale gas flow behavior using numerical simulation. SPE J. 20 (1), 142-154. https://doi.org/10.2118/
- Sun, J.L., Zou, A., Sotelo, E., et al., 2016. Numerical simulation of CO₂ huff-n-puff in complex fracture networks of unconventional liquid reservoirs. J. Nat. Gas Sci.

- Eng. 31, 481-492. https://doi.org/10.1016/j.jngse.2016.03.032.
- Taylor, R., Krishna, R., 1993. Multicomponent Mass Transfer. John Wiley & Sons. Tene, M., Bosma, S.B.M., Al Kobaisi, M.S., et al., 2017. Projection-based embedded discrete fracture model (pEDFM). Adv. Water Resour. 105, 205-216.
- Voskov, D.V., Tchelepi, H.A., 2012. Comparison of nonlinear formulations for twophase multi-component EoS based simulation. J. Pet. Sci. Eng. 82–83, 101–111. https://doi.org/10.1016/j.petrol.2011.10.012.
- Wang, B., Fidelibus, C., 2021. An open-source code for fluid flow simulations in unconventional fractured reservoirs. Geosciences 11 (2), 106. https://doi.org/ 10.3390/geosciences11020106.
- Wang, F.P., Reed, R.M., John, A., et al., 2009. Pore networks and fluid flow in gas shales. In: SPE Annual Technical Conference and Exhibition, https://doi.org/ 10.2118/124253-MS
- Wang, L., Tian, Y., Yu, X.Y., et al., 2017. Advances in improved/enhanced oil recovery technologies for tight and shale reservoirs. Fuel 210, 425-445. https://doi.org/ 10.1016/i.fuel.2017.08.095.
- Wang, Q., Jiang, R.Z., Cui, Y.Z., et al., 2020. Pre-Darcy flow behavior of CO2 Huff-n-Puff development in Fuyu tight formation: experiment and numerical evaluation. J. Pet. Sci. Eng. 186, 106773. https://doi.org/10.1016/j.petrol.2019.106773.
- Wang, Q., Jiang, R.Z., Leng, J., et al., 2021. The effect of the viscosity-dependent boundary layer on tight oil flow behavior in CO₂ Huff-Puff processes: a unified dimensional Pre-Darcy flow model. J. Pet. Sci. Eng. 204, 108718. https:// doi.org/10.1016/j.petrol.2021.108718.
- Wang, Q, Zhao, J.Z., Hu, Y.Q., et al., 2022. Shut-in time optimization after fracturing in shale oil reservoirs. Petrol. Explor. Dev. 49 (3), 671–683. https://doi.org/10.1016/S1876-3804(22)60056-9.
- Wang, X.K., Sheng, J.J., 2017. Effect of low-velocity non-Darcy flow on well production performance in shale and tight oil reservoirs. Fuel 190, 41-46. https:// doi.org/10.1016/j.fuel.2016.11.040.
- Wang, Y., Cao, R., Jia, Z., et al., 2024. A multi-mechanism numerical simulation model for CO₂-EOR and storage in fractured shale oil reservoirs. Petrol. Sci. 21 (3), 1814-1828. https://doi.org/10.1016/j.petsci.2024.02.006.
- Wasaki, A., Akkutlu, I.Y., 2015. Permeability of organic-rich shale. SPE J. 20 (6), 1384-1396. https://doi.org/10.2118/170830-PA
- Wu, K., Li, X., Guo, C., et al., 2016. A unified model for gas transfer in nanopores of shale-gas reservoirs: coupling pore diffusion and surface diffusion. SPE J. 21 (5), 1583-1611. https://doi.org/10.2118/2014-1921039-pa.
- Wu, Y.S., Li, J.F., Ding, D.Y., et al., 2014. A generalized framework model for the simulation of gas production in unconventional gas reservoirs. SPE J. 19 (5), 845-857. https://doi.org/10.2118/163609-PA.
- Yew, C.H., Weng, X., 2014. Mechanics of Hydraulic Fracturing. Gulf Professional **Publishing**
- Yu, W., Wu, K., Liu, M., et al., 2018. Production forecasting for shale gas reservoirs with nanopores and complex fracture geometries using an innovative nonintrusive EDFM method. In: SPE Annual Technical Conference and Exhibition. https://doi.org/10.2118/191666-MS
- Yu, W., Zhang, Y., Varavei, A., et al., 2019. Compositional simulation of CO2 huff 'n' puff in eagle ford tight oil reservoirs with CO2 molecular diffusion, nanopore confinement, and complex natural fractures. SPE Reservoir Eval. Eng. 22 (2), 492-508. https://doi.org/10.2118/190325-PA
- Zhang, F., Emami-Meybodi, H., 2020a. Flowback fracture closure of multi-fractured horizontal wells in shale gas reservoirs. J. Pet. Sci. Eng. 186, 106711. https:// doi.org/10.1016/j.petrol.2019.106711.
- Zhang, F., Emami-Meybodi, H., 2020b. A semianalytical method for two-phase flowback rate-transient analysis in shale gas reservoirs. SPE J. 25 (4), 1599-1622. https://doi.org/10.2118/201225-PA.
- Zhang, F., Emami-Meybodi, H., 2021. Analysis of early-time production data from multi-fractured shale gas wells by considering multiple transport mechanisms through nanopores. J. Pet. Sci. Eng. 197, 108092. https://doi.org/10.1016/ j.petrol.2020.108092.
- Zhang, F., Pan, Y., Liu, C., et al., 2024. A two-phase flowback type curve with fracture damage effects for hydraulically fractured reservoirs. SPE J. 29 (10), 5464-5486. https://doi.org/10.2118/215034-PA.
- Zhang, T., Li, X.F., Li, J., et al., 2017. Numerical investigation of the well shut-in and fracture uncertainty on fluid-loss and production performance in gas-shale reservoirs. J. Nat. Gas Sci. Eng. 46, 421-435. https://doi.org/10.1016/ j.jngse.2017.08.024.
- Zhao, X.R., Chen, Z.M., Wang, B., et al., 2023. A Multi-medium and Multi-mechanism model for CO₂ injection and storage in fractured shale gas reservoirs. Fuel 345, 128167. https://doi.org/10.1016/j.fuel.2023.128167.
- Zhao, Y., Rui, Z.H., Zhang, Z., et al., 2022. Importance of conformance control in reinforcing synergy of CO₂ EOR and sequestration. Petrol. Sci. 19 (6), 3088–3106. https://doi.org/10.1016/j.petsci.2022.09.036.
- Zia, H., Lecampion, B., 2017. Propagation of a height contained hydraulic fracture in turbulent flow regimes. Int. J. Solid Struct. 110, 265-278. https://doi.org/ 10.1016/j.ijsolstr.2016.12.029.
- Zolotukhin, A.B., Gayubov, A.T., 2021. Semi-analytical approach to modeling forchheimer flow in porous media at meso- and macroscales. Transport Porous Media 136 (3), 715-741. https://doi.org/10.1007/s11242-020-01528-4.